Modeling and Vision-Based Control of Large-Dimension Cable-Driven Parallel Robots Using a Multiple-Camera Setup

Tej Dallej, Marc Gouttefarde, Nicolas Andreff, Pierre-Elie Hervé, Philippe Martinet

To cite this version:

Tej Dallej, Marc Gouttefarde, Nicolas Andreff, Pierre-Elie Hervé, Philippe Martinet. Modeling and Vision-Based Control of Large-Dimension Cable-Driven Parallel Robots Using a Multiple-Camera Setup. Mechatronics, 2019, 61, pp.20-36. 10.1016/j.mechatronics.2019.05.004 . lirmm-02157768

HAL Id: lirmm-02157768
https://hal-lirmm.ccsd.cnrs.fr/lirmm-02157768

Submitted on 17 Jun 2019

Modeling and Vision-Based Control of Large-Dimension Cable-Driven Parallel Robots Using a Multiple-Camera Setup

Tej Dallej[a], Marc Gouttefarde[b], Nicolas Andreff[a,c], Pierre-Elie Hervé[d], Philippe Martinet[a,e]

[a] *Institut Pascal, UBP/CNRS/SIGMA, Clermont-Ferrand, France, Email: tdallej@yahoo.fr*
[b] *LIRMM, Université de Montpellier, CNRS, Montpellier, France, Email: Marc.Gouttefarde@lirmm.fr*
[c] *Institut FEMTO-ST, Univ. Bourgogne Franche-Comté/CNRS, Besançon, France.*
[d] *Tecnalia France, 950 rue Saint-Priest, Montpellier, France.*
[e] *CHORALE team, Inria CRISAM, Sophia Antipolis, France.*

Abstract

This paper deals with the modeling and vision-based control of large-dimension cable-driven parallel robots. Inverse kinematics and instantaneous inverse kinematics models are derived from the elastic catenary cable modeling. These models turn out to be dependent on the pose of the mobile platform (end-effector), on the cable tangent directions and on the cable tensions. In order to control the motion of the robot, a position-based visual servo control is used, where the mobile platform pose is measured by vision and used for regulation. A multi-camera setup and load cells provide the aforementioned desired measurements, i.e., the mobile platform pose, the directions of the tangents to the cables, and the cable tensions. The proposed approach was validated in experiments on the large-dimension cable-driven parallel robot prototype CoGiRo of global dimensions 15 m x 11 m x 6 m (L x l x h). A maximum error of less than 1 cm in position and 0.5° in orientation was achieved. Moreover, in the case of cable-driven parallel robots larger than the prototype CoGiRo, simulations were conducted in order to assess the influence on the vision-based control of four instantaneous inverse kinematics models.

Keywords: Cable-Driven Parallel Robots, Visual Servoing, Kinematics

---

1. Introduction

Most existing parallel robots [1, 2] are designed with rigid legs which cannot exceed a certain length. A major drawback of such designs is their limited workspace. Cable-Driven Parallel Robots (CDPRs) are a particular type of parallel robot in which cables connect the base to the mobile platform [1, 3]. Their main advantage may be scalability: Cables with small to very large lengths are easily stored on winch drums allowing one to build CDPRs with a workspace of global dimension ranging from a few centimeters [4] to tens of meters or more [5]. This useful property makes CDPRs good candidates for several applications, e.g., robotic cranes [6], automated construction systems [7], aerial camera systems [8], human-scale force-feedback haptic systems [9], or large radio telescopes [10, 11].

The context of the work presented in this paper is the displacement of heavy payloads by means of a CDPR operating at low velocities within a large workspace. Such heavy payload displacements are relevant in a number of applications in the lifting, construction and other heavy industries, where low velocities may be required, or preferred, for safety reasons. Consequently, this work focuses on large-dimension CDPRs whose dynamics is disregarded in their control since quasi-static operation is assumed.

CDPRs have a relatively low positioning accuracy which is often an issue in the aforementioned applications. Sensor-based control, and in particular visual servoing (vision-based control), is one possible means of improving accuracy while another means consists in improving the CDPR modeling used in an open-loop control of the mobile platform pose. On the one hand, vision may be difficult to implement in some industrial environments notably because of possible occlusions and lighting variations. Moreover, it requires the use of one or several cameras and usually of a number of visual targets. Nevertheless, on the other hand, by using

Paper published in Mechatronics, Vol. 61, pp. 20-36

direct measurements of the CDPR mobile platform pose in Cartesian space, visual servoing does not fully rely on model-based open-loop calculations to improve accuracy of CDPRs. Hence, robustness to modeling uncertainties and errors, to payload modifications, and to changes in some environmental conditions (e.g. temperature) can be significantly improved. Among other difficulties related to accurate CDPR modeling, cable elasticity, whose modeling and identification is often an issue in practice e.g. [12–16][1], can notably be avoided. Hence, it is worth investigating the use of visual servoing to accurately control the pose of the mobile platform of large-dimension CDPRs.

In the framework of Cartesian space control, assuming accurate enough cable length estimations, the pose of the CDPR mobile platform can be determined by means of forward kinematics, e.g. [17]. However, the latter is generally difficult to solve especially when the cable mass is taken into account [18] or when some of the cables are slack [19]. For massless cables, forward kinematics can be simplified by using additional information such as an estimation of the mobile platform orientation by means of an inertial measurement unit [20]. Nevertheless, cable length estimation is still required which can be an issue for large-dimension heavy payload CDPRs. An alternative is to use additional passive cables setting up an independent metrology [21] and whose layout is such that the forward kinematics has closed-form solutions but this solution increases the probability of cable collisions and adds constraints to the mechanical design. Cable angle sensors were recently proposed as a means to simplify forward kinematics and were applied to simple CDPRs [22, 23]. Their use for large-dimension 6-DOF CDPRs should be relevant but, to the best of our knowledge, it has not yet been reported and is thus an open issue. Overcoming these difficulties, vision allows the replacement of the forward kinematics by a direct estimation of the mobile platform pose obtained by measurements of the positions of visual targets fixed to the CDPR mobile platform.

Vision-based control of CDPRs has been considered in some previous works. In [24], the authors proposed a robust PD control using adaptive compensation for fully-constrained CDPRs. It was validated on a small-size low-payload point-mass planar CDPR whose position was measured by a CCD camera. The cables were considered to be massless and inextensible. Using a 3D pose kinematic visual servoing, in which the mobile platform pose is used for regulation, the work reported in [25] confirmed that visual servoing techniques [26–28] are a good alternative for the control of CDPRs. In [25], the cables were supposed to be massless and inextensible, a single camera was placed in front of the robot and a pattern was fixed to the end-effector (eye-to-hand configuration). Thereby, the instantaneous inverse kinematic model depends only on the pose of the mobile platform and on some constant (calibration) parameters. Later in [29], using a motion-capture system, a similar position-based visual servo control was used to ensure an accurate positioning of the mobile platform of the CDPR INCA 6D which has a cubic configuration of 3 m side length. An accuracy of less than 1 mm in position and 1° in orientation was obtained. In [30], a camera is used to measure and close the loop on the pose of the mobile platform of a small-size planar fully-constrained CDPR while, in [31], the camera is combined with three laser sensors to close the loop on the mobile platform pose of a small-size 6-cable suspended CDPR. Recently, [32] contributed an alternative approach to the standard computed torque control and applied it to a small-size planar suspended CDPR with highly flexible cables where pose and velocity feedback was provided by a 500 Hz camera placed in front of the CDPR and an embedded IMU. Along a square reference trajectory of 21 cm × 21 cm, an accuracy of 1.7 mm and 7.8 mrad was obtained. Besides, a camera mounted on the mobile platform of a CDPR was used in [8, 20, 33–35]. The camera was not used for feedback control purposes in [8, 20, 33]. In [34], an image-based visual servo control with an eye-in-hand configuration allowed the Marionet-Assist CDPR to grasp and move an object. In a workspace of 4 x 3 x 3 [m], a positioning accuracy of the order of 1 cm was obtained (the orientation was not controlled). [35] reports an experiment with a 4-cable CDPR following a straight line trajectory of two meters. A camera on-board the mobile platform detects lines at known positions in the workspace leading to a mean positioning error of 8.8 mm.

In these previous works and in many other studies devoted to the control of CDPRs, e.g. [30, 36–41], the cables are considered as being straight line segments. A few works investigate the control of large-dimension CDPRs [10, 42–44] but even fewer take cable sagging into account [11, 45–47]. In fact, in the case

---

[1] in [12], refer to Sections 3.8.5 and 3.8.6

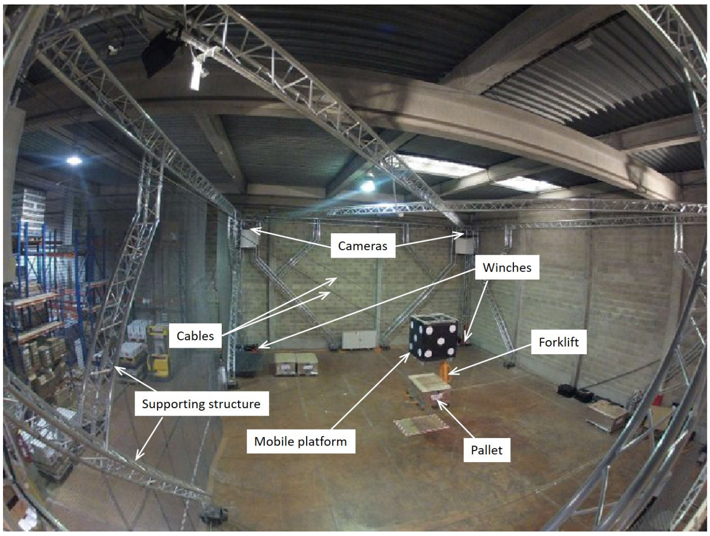

Figure 1: The LIRMM/Tecnalia 6-DOF CDPR CoGiRo of global dimensions 15 m x 11 m x 6 m (length x width x height).

of large-dimension CDPRs or of CDPRs designed to handle heavy payloads according to Standards [48], where a factor of safety is used in the selection of the cable, the cable mass is non-negligible [49, 50] and the cables may sag under their own weight, especially when steel cables are used. The dynamics of CDPRs simulated with lumped mass or continuous mass cable modeling, e.g. [51–53], have recently attracted more interests. However, since quasi-static operation is assumed in the present work, the classic elastic catenary cable model [5] is considered in order to take into account the cable mass and elasticity. Because the corresponding inverse kinetostatic problem is difficult to solve in real-time, assuming that the cable sag is relatively small, a simplified modeling of cables of non-negligible mass can be considered [54]. Compared to the use of the full elastic catenary cable model, it leads to a simplified static analysis of large-dimension CDPRs [47, 55] which is of significant interest for real-time control purposes and for vibration analysis [53].

The overall contribution of the present work is the application of vision-based control to large-dimension CDPRs with sagging cables, aiming at accurate positioning of the mobile platform. Based on the analysis presented in [47, 55], the cable sagging is taken into account by means of original inverse kinematics and instantaneous inverse kinematics models. These models turn out to be dependent on the mobile platform pose, on the directions of the tangents to the cables at their drawing points and on the cable tensions. In the case of large-dimension CDPRs, it is not conceivable to measure all the needed variables using a single camera so that the proposed vision-based control strategy uses a multi-camera perception system. In the present work, three cameras fixed to the robot base frame were used, providing a wide field of view and an accurate pose estimation. Moreover, by locally observing each cable by means of a stereo pair (two cameras), 3D reconstruction yields the directions of the tangents to the cables at their drawing points. Finally, the cable tensions are obtained by means of force sensors (load cells). Using this multi-camera setup together with a position-based visual servo control, the proposed approach has been validated in experiments on the 6-DOF large-dimension CDPR CoGiRo (Fig. 1). A maximum error of less than 10 mm in position and 0.5° in orientation has been achieved. This contribution is further illustrated in Tab. 1 where several relevant previous works are compared. It can notably be seen that vision-based control of such a large CDPR was never done before and that accounting for the cable mass is not common. Moreover, the relevance of the approach proposed in this paper is supported by the obtained positioning accuracy which, being given the dimensions and the platform and payload mass of the CDPR CoGiRo, are very satisfactory compared to previous works. Indeed, the two previous works on large-dimension CDPRs having a better ratio of accuracy to dimension (last column in Tab. 1) are [11] and [10]. In [11], an absolute accuracy of 100 mm (versus 10 mm in the present work) has been obtained by means of differential GPS while in [10], the absolute accuracy is better (1 mm) but at the cost of using very costly equipment[2]. Consequently, compared to the previous works in Tab. 1, the vision-based control approach proposed in the present paper represents the best trade-off between workspace size, relative/absolute accuracy, practicalities and cost.

Let us note that an instantaneous inverse kinematics model and the corresponding vision-based control was already presented in a preliminary work by the authors [56] where it was validated in simulation only. In the present work, the vision-based control strategy has been implemented and validated experimentally on the 6-DOF large-dimension CDPR CoGiRo. In addition to these experiments, the feasibility of the proposed approach on CDPRs larger than CoGiRo is assessed in simulations by comparing performances obtained with various inverse kinematics models. Experimental and simulation results indicate that taking cable sagging into account in the proposed vision-based control allows performances to be improved, especially in the case of very large CDPRs.

This paper is organized as follows. In Section 2, based on the elastic catenary cable model, inverse kinematics models are obtained from a generic expression of the cable unstrained length. In Section 3, the corresponding instantaneous inverse kinematics models are derived. Section 4 is dedicated to the multi-camera setup and Section 5 presents the position-based visual servo control. Experimental validations on the large-dimension 6-DOF CDPR CoGiRo are discussed in Section 6. Section 7 presents simulation results where four instantaneous inverse kinematics models are compared. Conclusions are finally drawn in Section 8.

---

[2] three laser automatic total stations and 2 laser trackers

	CDPR largest dimension	Cable sagging	Cable elasticity	Pulley kinematics	Load and platform mass	Type of sensors	Absolute accuracy	Ratio
Present work (CoGiRo)	**15 m**	Yes	No	No	**210 kg**	Multi-camera setup and force sensors	**10 mm** **0.5 deg**	**0.07 %**
[11]	**730 m**	No	No	No	**17.9 kg**	Differential GPS	**100 mm**	**0.014 %**
[12] (IPAnema3)	16 m	No	Yes	Yes	25 kg	Winch encoders	40 mm	0.25 %
[44] (IPAnema2)	7 m	No	Yes	Yes	n/a	Winch encoders	34 mm	0.49 %
[47] (CoGiRo)	15 m	Yes	Yes	No	210 kg	Winch encoders	39.6 mm	0.26 %
[10]	**50 m (workspace 10 m)**	No	No	No	**450 kg**	Total stations and laser trackers	**1 mm** **0.11 deg (rms)**	**0.002 %**
[46]	5 m	Yes	Yes	No	20 kg	Winch encoders	100 mm	2 %
[29] (INCA 6D)	3 m	No	No	No	n/a	Motion capture syst.	1 mm 1 deg	0.033 %
[34] (Marionet Assist)	4 m	No	No	No	n/a	Camera	10 mm	0.25 %
[35]	4.5 m	No	Yes	No	14 kg	Camera	8.8 mm	0.2 %
[57]	n/a	No	No	No	0.115 kg	Cable angle sensors and Winch encoders	12.5 mm	n/a
[58]	3 m	No	Yes	No	14.5 kg	IMU	n/a	n/a
[31] (ICaSbot)	1.2 m	No	Yes	No	1.1 kg	Camera, lasers and load cells	$\simeq$ 10 mm	0.83 %
[30] (KNTU)	2.24 m	No	No	No	2.5 kg	Camera and load cells	8 - 45 mm 1.7 deg	0.35 - 2 %

Table 1: Comparison to some relevant previous works. The column "cable sagging" (resp. "cable elasticity", "pulley kinematics") reports whether or not sagging (resp. elasticity, pulley kinematics) is used in the CDPR control. The given absolute accuracy values are indicative and one should refer to the corresponding bibliographic reference for details on the meaning of each of these values. The last column (Ratio) gives the ratio of the absolute positioning accuracy to the CDPR largest dimension.

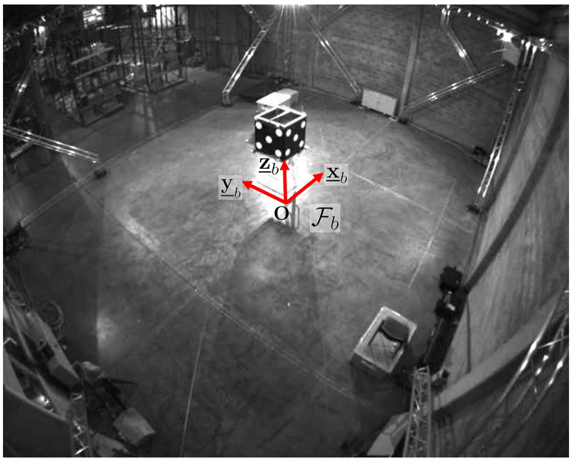

Figure 2: The initial position of the mobile platform of the CDPR CoGiRo seen from the first camera used to measure the pattern positions. Each pattern consists of five visual targets (white points). Four such patterns are attached to the four lateral faces of the CDPR mobile platform. The frame $\mathcal{F}_b$ shown in the figure is the CDPR reference frame fixed to the ground.

2. Elastic Catenary and Inverse Kinematics Models

Several fixed and mobile coordinate frames are used in this paper. The following fixed coordinate frames are first defined.

- $\mathcal{F}_b = (\mathbf{O}, \underline{\mathbf{x}}_b, \underline{\mathbf{y}}_b, \underline{\mathbf{z}}_b)$ is the CDPR reference frame as shown in Fig. 2. The CDPR CoGiRo global dimensions are 15 m x 11 m x 6 m (length x width x height). As shown in the figure, the vectors $\underline{\mathbf{x}}_b$, $\underline{\mathbf{y}}_b$, and $\underline{\mathbf{z}}_b$ are directed along the length, width, and height of CoGiRo. The origin $\mathbf{O}$ is located at the center of the footprint of CoGiRo, a few centimeters above the ground.

- Another fixed reference frame $\mathcal{F}_f = (\mathbf{O}_f, \underline{\mathbf{x}}_f, \underline{\mathbf{y}}_f, \underline{\mathbf{z}}_f)$ is used in the sequel. It is the frame fixed to one of the three cameras installed on the CDPR base frame and used to estimate the mobile platform pose. The picture shown in fig. 2 has been taken by this camera.

- The cable i reference frame $\mathcal{F}_{Ai} = (\mathbf{A}_i, \underline{\mathbf{x}}_{Ai}, \underline{\mathbf{y}}_{Ai}, \underline{\mathbf{z}}_{Ai})$ is fixed to the vertical plane Π_i which contains cable i when the latter is in static equilibrium as shown in Fig. 4. $\mathbf{A}_i$ is the point wherefrom cable i extends from the CDPR base frame (cable drawing point). Vector $\underline{\mathbf{z}}_{Ai}$ is vertical.

Moreover, the following mobile coordinate frames are also defined.

- $\mathcal{F}_e = (\mathbf{E}, \underline{\mathbf{x}}_e, \underline{\mathbf{y}}_e, \underline{\mathbf{z}}_e)$ denotes the frame attached to the CDPR mobile platform, where $\mathbf{E}$ is the mobile platform reference point. In the orientation of the mobile platform of CoGiRo shown in Fig. 2, $\mathcal{F}_e$ has the same orientation as $\mathcal{F}_b$.

- Four patterns, each consisting of five visual targets (white points), are attached to the four lateral faces of the CDPR mobile platform. Two of these four patterns are visible in Fig. 2. The pattern visual target positions are expressed in $\mathcal{F}_m$ which is another frame attached to the CDPR mobile platform. Note that frame $\mathcal{F}_m$ is different from frame $\mathcal{F}_e$ for geometric calibration purposes.

These fixed and mobile coordinate frames are shown in Fig. 3. In the sequel, ${}^j\mathbf{v}$ denotes a generic vector $\mathbf{v}$ expressed in frame $\mathcal{F}_j$.

Fig. 4 shows the profile of cable i with non-negligible mass, where $i = 1...k$, and k is the number of cables. In static equilibrium, the cable lies in the vertical plane Π_i containing the base point $\mathbf{A}_i = (A_{ix}\ A_{iy}\ A_{iz})^T$ and the platform point $\mathbf{B}_i = (B_{ix}\ B_{iy}\ B_{iz})^T$. $\mathbf{A}_i$ and $\mathbf{B}_i$ are the position vectors of the two extremities of the sagging part of cable i, i.e., $\mathbf{B}_i$ is the cable attachment point on the mobile platform and $\mathbf{A}_i$ is the cable drawing point. The frame $\mathcal{F}_{Ai} = (\mathbf{A}_i, \underline{\mathbf{x}}_{Ai}, \underline{\mathbf{y}}_{Ai}, \underline{\mathbf{z}}_{Ai})$, attached to plane Π_i, is obtained from the base frame

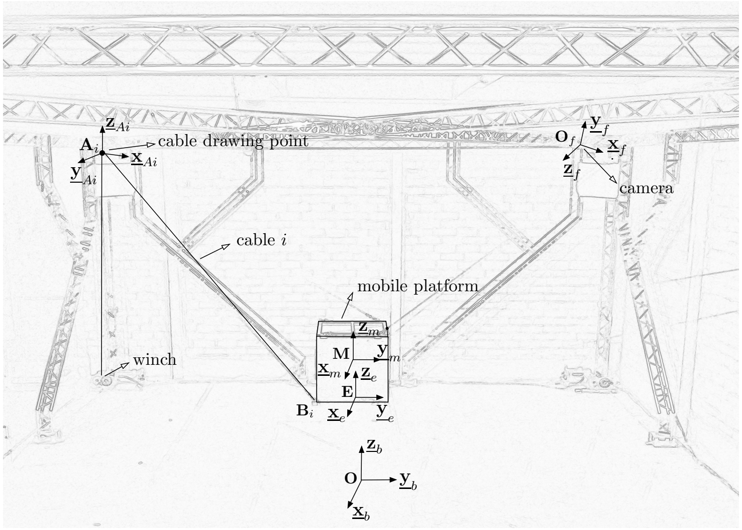

Figure 3: The fixed and mobile coordinate frames used in this paper.

$\mathcal{F}_b$ by a rotation of angle γ_i around the z axis ($\underline{\mathbf{z}}_b = \underline{\mathbf{z}}_{Ai}$ being vertical). Let $\underline{\mathbf{u}}_i$ be the unit vector from $\mathbf{A}_i$ to $\mathbf{B}_i$. The angle γ_i can be computed as:

$$\gamma_i = tan^{-1}\left(\frac{{}^b u_{iy}}{{}^b u_{ix}}\right) \tag{1}$$

where ${}^b\underline{\mathbf{u}}_i = \left({}^b u_{ix}, {}^b u_{iy}, {}^b u_{iz}\right)^T$ is the unit vector $\underline{\mathbf{u}}_i$ expressed in frame $\mathcal{F}_b$.

As shown in Fig. 4, a point $\mathbf{M}_i(s_i)$ on the cable profile has two non-zero Cartesian coordinates x_i and z_i in frame $\mathcal{F}_{Ai}$. s_i denotes the unstrained length of the cable segment between $\mathbf{A}_i$ and $\mathbf{M}_i$ so that $0 \leq s_i \leq l_i$, where l_i is the unstrained length of cable i. Hence, $\mathbf{M}_i$ corresponds to point $\mathbf{A}_i$ when $s_i = 0$ and to point $\mathbf{B}_i$ when $s_i = l_i$. The elastic catenary cable model (ECM) [5, 54] is considered in this paper. It accounts for both the cable mass and elasticity. Using the well-known catenary equations ($x_i(s_i)$ and $z_i(s_i)$) presented in [54] and assuming that the cable elasticity has a little influence on the cable shape, it has been shown in [47] that:

$$z_i(x_i) = \frac{1}{\mu_i}(\cosh(\mu_i x_i + a_i) - \cosh(a_i)) \tag{2}$$

where

- $\mu_i = \frac{\rho_0 g}{{}^{Ai}\vartheta_{Bix}}$, ρ_0 is the linear mass density of each cable and g the acceleration of gravity
- ${}^{Ai}\vartheta_{Bix}$ is the x-component in the cable frame $\mathcal{F}_{Ai}$ of the force $\boldsymbol{\vartheta_{Bi}}$ applied to the cable at its attachment point $\mathbf{B}_i$
- $a_i = \ln\left(\frac{\mu_i {}^{Ai}B_{iz} + \sqrt{(\mu_i {}^{Ai}B_{iz})^2 + e^{\mu_i {}^{Ai}B_{ix}} + e^{-\mu_i {}^{Ai}B_{ix}} - 1}}{e^{\mu_i {}^{Ai}B_{ix}} + e^{-\mu_i {}^{Ai}B_{ix}} - 1}\right)$, for ${}^{Ai}B_{ix} > 0$ and ${}^{Ai}\vartheta_{Bix} > 0$

From (2), the following equation can be obtained [47]:

$$\frac{ds_i}{dx_i} = \frac{EA_0}{{}^{Ai}\vartheta_{Bix}}\left(1 - \frac{1}{1 + R_i}\right) \tag{3}$$

where $R_i = \frac{{}^{Ai}\vartheta_{Bix}}{EA_0}\cosh(\mu_i x_i + a_i)$, E [Pa] is the cable elastic modulus and A_0 [m^2] the cable cross-section area.

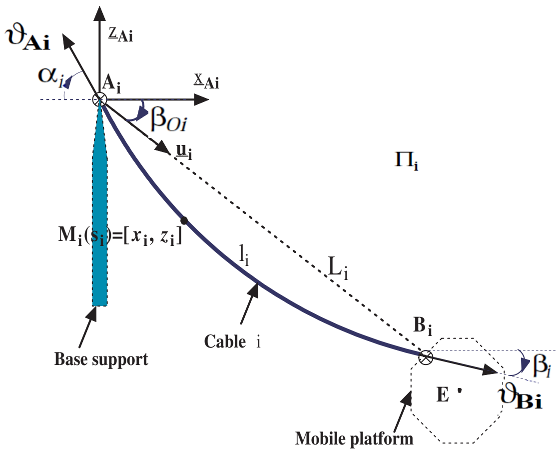

Figure 4: Static equilibrium of cable i having non-negligible mass.

2.1. Tangents to the cable profile

The slope of the tangents to the cable profile (Eq. (2)) at points $\mathbf{B}_i$ and $\mathbf{A}_i$ (see Fig. 4) can be computed using $\frac{dz_i}{dx_i}_{(x_i=B_{ix})} = \tan(\beta_i)$ and $\frac{dz_i}{dx_i}_{(x_i=0)} = \tan(\alpha_i)$, respectively. According to (2), one can write:

$$\begin{cases} \tan(\beta_i) = \frac{^{Ai}\vartheta_{Biz}}{^{Ai}\vartheta_{Bix}} = \sinh(\mu_i {}^{Ai}B_{ix} + a_i) \\ \tan(\alpha_i) = \frac{^{Ai}\vartheta_{Aiz}}{^{Ai}\vartheta_{Aix}} = \sinh(a_i) \end{cases} \tag{4}$$

The angle β_{0i} between $\underline{\mathbf{u}}_i$ and $\underline{\mathbf{x}}_{Ai}$ (Fig. 4), which is the angle between the cable direction and the horizontal when the cable mass is neglected, can be written as:

$$\tan(\beta_{0i}) = \frac{^{Ai}B_{iz}}{^{Ai}B_{ix}} \tag{5}$$

2.2. Inverse kinematics

The inverse kinematics (IK) calculates the unstrained length of each cable for a given pose of the platform. Using Eq. (3), the unstrained cable length can be calculated by integrating a cable length element to obtain the following expression:

$$\begin{aligned} l_{ECM_i} = l_i &= \int_0^{^{Ai}B_{ix}} \frac{ds_i}{dx_i}\,\mathrm{d}x_i = \int_0^{^{Ai}B_{ix}} \frac{EA_0}{^{Ai}\vartheta_{Bix}} \sum_{j=1}^{O_l} (-1)^{(j-1)} (R_i)^j \,\mathrm{d}x_i \\ &= \sum_{j=1}^{O_l} \left(^{Ai}\vartheta_{Bix}\right)^j \left(-\frac{1}{2EA_0}\right)^{(j-1)} \left(\sum\nolimits_{i1} + S_j \frac{C_j^{k_p}\, {}^{Ai}B_{ix}}{2^{Ai}\vartheta_{Bix}}\right) \end{aligned} \tag{6}$$

where

- O_l is the order of the series expansion of $\frac{ds_i}{dx_i}$, and $\sum\limits_{j=1}^{O_l} (-1)^{(j-1)} (R_i)^j$ is the series expansion of $1 - \dfrac{1}{1+R_i}$
- $\sum_{i1} = \sum\limits_{k=0}^{k_p-1} \dfrac{C_j^k}{\rho_0 g (j-2k)} \big(\sinh((j-2k)(\mu_i {}^{Ai}B_{ix} + a_i)) - \sinh((j-2k)a_i)\big)$
- $S_j = 1$ and $k_p = \frac{j}{2}$ if j is an even number, while $S_j = 0$ and $k_p = \frac{j-1}{2}$ if j is an odd number
- $C_j^k = \frac{j!}{k!(j-k)!}$

Model	Cable length l_i
Elastic Catenary Model (ECM)	l_{ECM_i} (refer to Eq. (6))
Catenary Model Without Elasticity (CMWE)	l_{CMWE_i} (refer to Eq. (7))
Simplified Catenary Model Without Elasticity (SCMWE)	l_{SCMWE_i} (refer to Eq. (8))
Straight Line Segment Model (SLSM)	l_{SLSM_i} (refer to Eq. (9))

Table 2: Relevant particular cases deduced from Elastic Catenary Model (ECM)

In Eq. (6), both the cable mass and elasticity are taken into account. To the best of our knowledge, the IK given in Eq. (6) is original in the sense that it is a generalization of previously proposed IK solutions and notably the one presented in [47]. In the framework of vision-based control, estimating the cable elongations is not of primary importance to positioning accuracy since the mobile platform pose is measured by vision. The following three particular cases, where cable elasticity is neglected, are thus of interest. These three cases, summarized in Tab. 2, can be deduced from the generic expression (6).

2.2.1. Catenary Model Without Elasticity (CMWE)

When $O_l = 1$ in (6) (first order series expansion), the terms containing the elastic modulus E disappear. Hence, $O_l = 1$ in (6) corresponds to the case where the cable elasticity is neglected and only the cable mass is taken into account. The cable unstrained length expression thereby obtained is consistent with the one in [47]:

$$l_{CMWEi} = \frac{1}{\mu_i} \left(\sinh(\mu_i {}^{Ai}B_{ix} + a_i) - \sinh(a_i) \right) \tag{7}$$

2.2.2. Simplified Catenary Model Without Elasticity (SCMWE)

Assuming that the cable sag is relatively small, a simplified modeling of the profile of a cable of non-negligible mass [54, 55] can be computed. This model consists of a parabolic cable profile equation and can be obtained from Eq. (7) by means of further assumptions as detailed in [47]. Using this parabolic cable profile equation, the cable length is computed as [55]:

$$\begin{aligned} l_{SCMWEi} &= \int_0^{{}^{Ai}B_{ix}} \sqrt{1 + (\tfrac{dz}{dx})^2}\, \mathrm{d}x \\ &= {}^{Ai}B_{ix} \frac{c_{1i}k_{1i} - c_{2i}k_{2i} + \ln\left(\frac{c_{1i}+k_{1i}}{c_{2i}+k_{2i}}\right)}{2r_i} \end{aligned} \tag{8}$$

where $r_i = \frac{\rho_0 g L_i}{{}^{Ai}\vartheta_{Bix}}$, $k_{1i} = \tan(\beta_{0i}) + \frac{r_i}{2}$, $k_{2i} = \tan(\beta_{0i}) - \frac{r_i}{2}$, $c_{1i} = \sqrt{1 + k_{1i}^2}$, $c_{2i} = \sqrt{1 + k_{2i}^2}$, and L_i is the length of the straight line segment A_iB_i.

2.2.3. Straight Line Segment Model (SLSM)

In this case, each cable is approximated as a straight line segment, the mass and elasticity of the cable being neglected (rigid massless cable model). The Taylor series expansion of order 0 of (7) around the expansion point $\mu_i {}^{Ai}B_{ix} \simeq 0$ and $\tan(\beta_i) \simeq \tan(\beta_{0i})$ gives:

$$l_{SLSMi} = {}^{Ai}B_{ix} \sqrt{1 + \tan(\beta_{0i})^2} = L_i \tag{9}$$

3. Instantaneous Inverse Kinematics Model

The instantaneous inverse kinematics model (IIKM) of a CDPR establishes the relationship between the mobile platform Cartesian velocity $\boldsymbol{\tau}_e$ (twist) and the time derivatives $\dot{\mathbf{l}} = (\ \dot{l}_1 \ \ ... \ \ \dot{l}_k\ )^T$ of the cable lengths. The mobile platform Cartesian velocity (linear and angular velocities) expressed in the fixed reference frame $\mathcal{F}_f$ is:

$${}^f\boldsymbol{\tau}_e = {}^f\boldsymbol{\tau}_{e/f} = (\ {}^f\mathbf{V}_{e/f}^T \quad {}^f\boldsymbol{\Omega}_{e/f}^T\ )^T \tag{10}$$

Model	IIKM
Elastic Catenary Model (ECM)	$\mathbf{N}_i$ (refer to Eq. (11))
Catenary Model Without Elasticity (CMWE)	$\mathbf{N}_i$ with $O_l = 1$
Simplified Catenary Model Without Elasticity (SCMWE)	$\mathbf{N}_i = (N_{i1} \ \ 0 \ \ N_{i2} \ \ N_{i3})$ (refer to [56])
Straight Line Segment Model (SLSM)	$\mathbf{N}_i =$ $(\cos(\beta_{0i}) \ \ 0 \ \ \sin(\beta_{0i}) \ \ 0)$ using $O_l = 1$, $\mu_i{}^{Ai}B_{ix} \simeq 0$ and $\tan(\beta_i) \simeq \tan(\beta_{0i})$

Table 3: Relevant particular cases deduced from the instantaneous inverse kinematics model (IIKM) in Eq. (11). The column IIKM indicates how matrix $\mathbf{N}_i$ is calculated for each model.

where ${}^j\boldsymbol{\tau}_{i/k}$ is the Cartesian velocity (linear and angular velocities ${}^j\mathbf{V}_{i/k}$ and ${}^j\boldsymbol{\Omega}_{i/k}$) of $\mathcal{F}_i$ with respect to $\mathcal{F}_k$ and expressed in $\mathcal{F}_j$, whereas ${}^j\boldsymbol{\tau}_i = {}^j\boldsymbol{\tau}_{i/j}$ is the Cartesian velocity of $\mathcal{F}_i$ expressed in and with respect to $\mathcal{F}_j$.

Differentiating (6) with respect to time gives:

$$\dot{l}_i = \mathbf{N}_i \begin{pmatrix} {}^{Ai}\dot{\mathbf{B}}_i \\ {}^{Ai}\dot{\vartheta}_{Bix} \end{pmatrix} \tag{11}$$

where

- $\mathbf{N}_i = \begin{pmatrix} N_{i1} & 0 & N_{i2} & N_{i3} \end{pmatrix}$
- $N_{i1} = \sum\limits_{j=1}^{O_l} \left(-\frac{\vartheta_{Bix}}{2EA_0}\right)^{(j-1)} \left(\sum_{i2} - \sinh(\mu_i{}^{Ai}B_{ix} + a_i) \sum_{i3} + S_j \frac{C_j^{k_p}}{2}\right)$
- $N_{i2} = \sum\limits_{j=1}^{O_l} \left(-\frac{\vartheta_{Bix}}{2EA_0}\right)^{(j-1)} \sum_{i3}$
- $N_{i3} = \sum\limits_{j=1}^{O_l} \Big(-\frac{\vartheta_{Bix}}{2EA_0})^{(j-1)} \Big(\frac{{}^{Ai}B_{ix} \sinh(\mu_i{}^{Ai}B_{ix} + a_i) - {}^{Ai}B_{iz}}{{}^{Ai}\vartheta_{Bix}} - \frac{{}^{Ai}B_{iz}}{{}^{Ai}\vartheta_{Bix}}\Big) \sum_{i3}$
  $- \frac{{}^{Ai}B_{ix}}{{}^{Ai}\vartheta_{Bix}} \sum_{i2} + j \sum_{i1} + S_j \frac{C_j^{k_p}\,{}^{Ai}B_{ix}}{2^{Ai}\vartheta_{Bix}}\Big)$
- $\sum_{i2} = \sum\limits_{k=0}^{k_p-1} C_j^k \cosh\big((j-2k)(\mu_i{}^{Ai}B_{ix} + a_i)\big)$
- $\sum_{i3} = \sum\limits_{k=0}^{k_p-1} C_j^k \frac{\cosh\big((j-2k)(\mu_i{}^{Ai}B_{ix} + a_i)\big) - \cosh\big((j-2k)a_i\big)}{\sinh\big(\mu_i{}^{Ai}B_{ix} + a_i\big) - \sinh(a_i)}$

Three relevant particular cases deduced from the instantaneous inverse kinematics model computed in (11) are given in Tab. 3. The instantaneous models in this table corresponds to the inverse kinematics models given in Tab. 2. The column IIKM in Tab. 3 indicates how matrix $\mathbf{N}_i$ is calculated for each model.

The time derivatives ${}^{Ai}\dot{\mathbf{B}}_i$ and ${}^{Ai}\dot{\vartheta}_{Bix}$ can be written as:

$${}^{Ai}\dot{\mathbf{B}}_i = \mathbf{D}_{Bi}{}^f\boldsymbol{\tau}_e, \quad {}^{Ai}\dot{\vartheta}_{Bix} = \mathbf{D}_{si}{}^f\boldsymbol{\tau}_e \tag{12}$$

where, according to the task function formalism [59], $\mathbf{D}_{Bi}$ and $\mathbf{D}_{si}$ are called interaction matrices. The expressions of these interaction matrices are given in Appendix A. With these notations, Eq. (11) becomes:

$$\dot{l}_i = \mathbf{D}_i{}^f\boldsymbol{\tau}_e \tag{13}$$

where $\mathbf{D}_i = \mathbf{N}_i \begin{pmatrix} \mathbf{D}_{Bi} \\ \mathbf{D}_{si} \end{pmatrix}$.

With the usual assumption that the cable length wound on the winch drum of a CDPR is the unstrained cable length, the time derivative of the vector $\mathbf{q}$ of the CDPR winch motor rotation angles is linearly related to the time derivatives of the cable lengths vector by $\dot{\mathbf{q}} = \frac{1}{r_c}\dot{\mathbf{l}}$, where r_c is the reduction ratio of the winches collecting the cables. Therefore, the instantaneous inverse kinematics associated with the motor angular velocities is:

$$\dot{\mathbf{q}} = \frac{1}{r_c}\mathbf{D}_a\,{}^f\boldsymbol{\tau}_e \tag{14}$$

where $\mathbf{D}_a$ is the compound matrix containing the matrices $\mathbf{D}_i$, $i = 1...k$.

4. A Multi-Camera Setup For Vision-Based Control

4.1. Measurement needs

In Section 5, the instantaneous inverse kinematics models introduced in the previous section are used within a vision-based control scheme. To this end, the parameters and variables on which this model depends should be identified in order to figure out the required measurements.

The instantaneous inverse kinematics model (14) depends on ${}^f\mathbf{T}_m$, the rigid transformation between the mobile frame $\mathcal{F}_m$ and the fixed frame $\mathcal{F}_f$. ${}^f\mathbf{T}_m$ is composed of a rotation matrix ${}^f\mathbf{R}_m$ and a translation vector ${}^f\mathbf{t}_m$ and defines the pose of the platform. It depends also on the unit vectors ${}^f\underline{\mathbf{u}}_{Ai}$ directing the tangents to the cables at their drawing points and on some constant (calibration) parameters (${}^e\mathbf{B}_i$, ${}^b\mathbf{A}_i$, ${}^m\mathbf{T}_e$ and ${}^f\mathbf{T}_b$). Additionally, to compute the instantaneous inverse kinematics model (14), the rotation matrix ${}^{Ai}\mathbf{R}_b$, which depends on the angle γ_i defined in (1), needs to be defined. This angle can also be computed using $\gamma_i = \tan^{-1}\left(\frac{{}^b u_{Aiy}}{{}^b u_{Aix}}\right)$, where ${}^b\underline{\mathbf{u}}_{Ai} = {}^b\mathbf{R}_f\,{}^f\underline{\mathbf{u}}_{Ai}$. The knowledge of the angle β_{0i} defined in (5) is also required. This angle can be computed using the following expressions of the attachment point $\mathbf{B}_i$:

$$\begin{cases} {}^{Ai}\mathbf{B}_i = {}^{Ai}\mathbf{R}_b({}^b\mathbf{R}_f\,{}^f\mathbf{B}_i + {}^b\mathbf{t}_f) + {}^{Ai}\mathbf{t}_b \\ {}^f\mathbf{B}_i = {}^f\mathbf{R}_m\,{}^m\mathbf{B}_i + {}^f\mathbf{t}_m \end{cases} \tag{15}$$

where ${}^m\mathbf{B}_i$ is a constant parameter.

The length $L_i = \| {}^f\overrightarrow{\mathbf{A}_i\mathbf{B}_i} \|$ of the straight line segment between $\mathbf{A}_i$ and $\mathbf{B}_i$ and the x-component ${}^{Ai}\vartheta_{Bix}$ of the force applied to the cable at its attachment point $\mathbf{B}_i$ are also required. L_i is straightforwardly obtained by means of ${}^m\mathbf{B}_i$, ${}^b\mathbf{A}_i$, ${}^f\mathbf{T}_m$ and ${}^f\mathbf{T}_b$. Moreover, ${}^{Ai}\vartheta_{Bix} = -{}^{Ai}\vartheta_{Aix}$ [5] where ${}^{Ai}\vartheta_{Aix}$ is the x-component of the force vector:

$${}^{Ai}\boldsymbol{\vartheta}_{Ai} = \vartheta_{Ai}\,{}^{Ai}\underline{\mathbf{u}}_{Ai} = \vartheta_{Ai}\,{}^{Ai}\mathbf{R}_b\,{}^b\mathbf{R}_f\,{}^f\underline{\mathbf{u}}_{Ai} \tag{16}$$

where ϑ_{Ai} is the tension in cable i at point $\mathbf{A}_i$.

In conclusion, apart from the constant coordinates of points ${}^e\mathbf{B}_i$ and ${}^b\mathbf{A}_i$ and constant transformations ${}^m\mathbf{T}_e$ and ${}^f\mathbf{T}_b$ which can be obtained by calibration (see Section 4.3) or from CAD modeling, the transformation ${}^f\mathbf{T}_m$, the unit vectors ${}^f\underline{\mathbf{u}}_{Ai}$ (directing the tangents to the cables at their drawing points) and the cable tensions ϑ_{Ai} are required. In this work, ${}^f\mathbf{T}_m$ and ${}^f\underline{\mathbf{u}}_{Ai}$ are measured by vision through a multi-camera setup and the tensions ϑ_{Ai} are given by tension sensors as presented in Section 4.2.

4.2. Description of a multi-camera setup

This section briefly describes a multi-camera setup installed on the CDPR CoGiRo [60] (Fig. 1). The latter is a 6-DOF large-dimension suspended CDPR of global dimensions 15 x 11 x 6 m (length x width x height). Its mobile platform has a 1 m^3 cubic structure connected to winches by 8 cables (two winches at the bottom of each of the four robot posts).

Using an eye-to-hand configuration, three cameras were installed at the top of the robot posts (Fig. 5). Four patterns, each consisting of five visual targets (white points), were attached to the four lateral faces of the cubic mobile platform as shown in Fig. 2. Thereby, the rigid transformation ${}^f\mathbf{T}_m$ from the fixed reference frame $\mathcal{F}_f$ to the mobile frame $\mathcal{F}_m$ can be found using the three cameras observing the visual

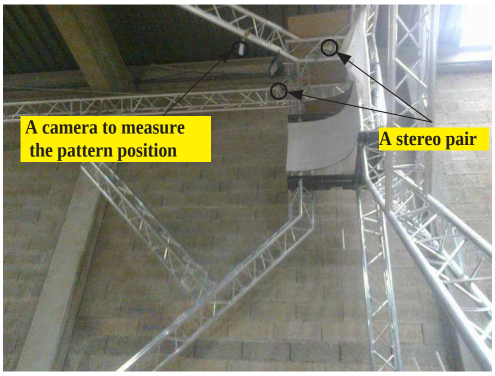

Figure 5: This figure shows the three cameras secured to the upper part of one of the four posts (top corner) of the supporting structure of the CDPR CoGiRo. Two of these three cameras form the stereo pair used to locally observe the two cables which exit the supporting structure at the top of this post. The stereo pair allows the 3D reconstruction of the directions of the tangents to the cables at their drawing points. Moreover, the third camera secured to the upper part of this post of the CDPR supporting structure is used to measure the pose of one of the four patterns attached to the CDPR mobile platform.

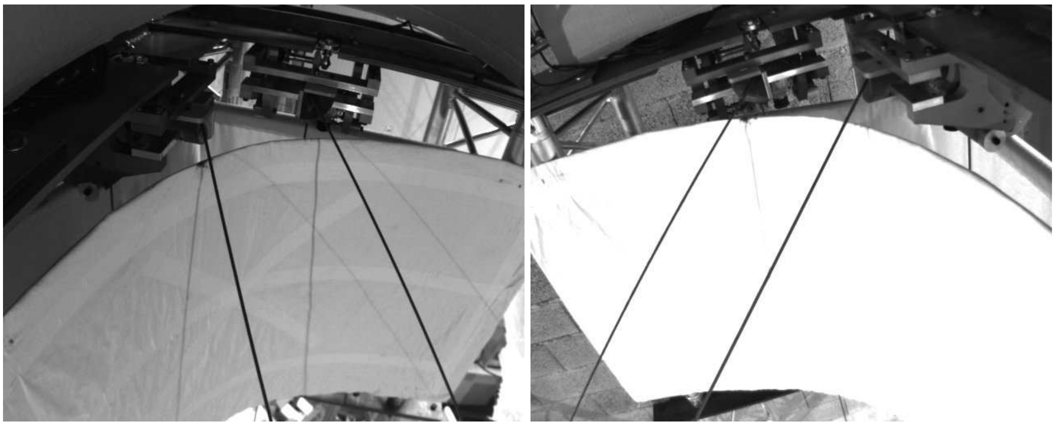

Figure 6: The two cables at their drawing points at each robot post, seen from the first stereo pair (left and right cameras).

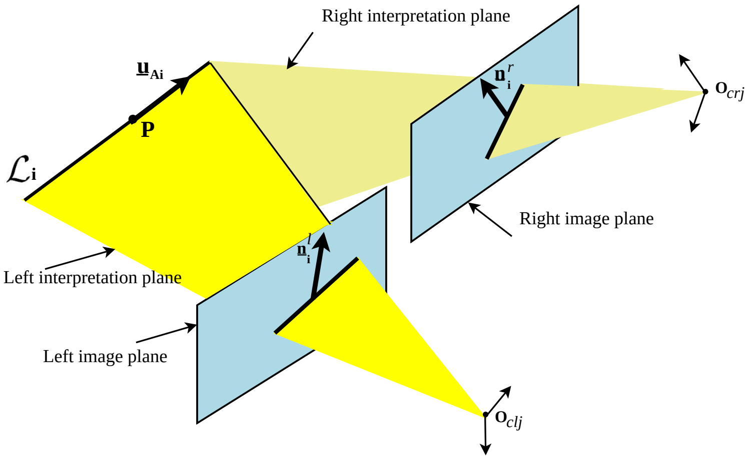

Figure 7: Projection of a 3D line in the image.

targets. Since several cameras observe several targets, ${}^f\mathbf{T}_m$ is computed using mean or average translations and rotations [61, 62]. Most existing CDPRs are designed with cables of small diameters. In the case at hand, the CDPR CoGiRo is driven by steel cables of diameter 4 mm. Then, the sagging cable can locally be approximated as a straight line segment for kinematics analysis. By locally observing each cable near its drawing point $\mathbf{A}_i$ by means of a stereo pair (a left camera and a right camera), the edges $\underline{\mathbf{n}}_i^l$ and $\underline{\mathbf{n}}_i^r$ associated to the line projection in the left image plane and in the right image plane, respectively, can be extracted (Fig. 6 and Fig. 7). The intersection of the image plane and the interpretation plane defines the perspective projection of the cable straight line segment $\mathcal{L}_i$ in the image planes. Thus, the line image projections could be represented by the normal to the interpretation planes $\underline{\mathbf{n}}_i^l$ and $\underline{\mathbf{n}}_i^r$. The direction $\underline{\mathbf{u}}_{Ai}$ for each tangent to the cable at its drawing point can then be computed as:

$$^{clj}\underline{\mathbf{u}}_{Ai} = \frac{^{clj}\underline{\mathbf{n}}_i^l \times {}^{clj}\underline{\mathbf{n}}_i^r}{\parallel {}^{clj}\underline{\mathbf{n}}_i^l \times {}^{clj}\underline{\mathbf{n}}_i^r \parallel} \tag{17}$$

where the left superscript clj denotes the frame associated to the j^{th} left camera of a stereo pair, $j = 1...r_c$ (r_c is the number of stereo pairs). As shown in Fig. 5 and 6, a white panel is installed behind the cables at each top corner of the supporting structure and spotlights are used to ensure an appropriate lighting. It allows the contrast and the visibility of the two cables to be increased and thus allows a proper tracking of the cable straight line segment $\mathcal{L}_i$.

In the present work, only four stereo pairs ($r_c = 4$) were needed to measure the eight cable directions $\underline{\mathbf{u}}_{Ai}$ since the eight cable drawing points of the robot CoGiRo are organized in four pairs, the two drawing points of each pair being close to each other (Fig. 6). Hence, with the 3 cameras observing the targets attached to the mobile platform, a total of 11 cameras have been used. Point and line tracking and the corresponding numerical computations were performed using ViSP [63], an open C++ library for visual servoing (Appendix B).

The last required measurements are the cable tensions ϑ_{Ai}. A total of 8 load cells have been used on the robot CoGiRo to estimate these cable tensions. The load cells were installed in the winches. Measurement noises required filtering in order to obtain cable tensions signals usable in the control. While the cable mass between the force sensor location in the winch and the drawing point $\mathbf{A}_i$ can be neglected, friction in the winch and at the cable drawing points, where eyelets were used, was significant and caused a difference between the measured winch-level cable tensions and the actual cable tensions ϑ_{Ai}.

4.3. Calibration process

The first step of the calibration process is to compute the intrinsic parameters of each camera and the extrinsic parameters of each pair of cameras used to measure the eight cable directions $\underline{\mathbf{u}}_{Ai}$. This step was performed using the Camera Calibration Toolbox in Matlab. Based on a total of 25 images of a planar checkerboard (camera calibration pattern), this tool estimates camera intrinsics, extrinsic, and lens distortion parameters.

The second step of the calibration process is to estimate the constant (calibration) parameters ${}^b\mathbf{A}_i$ and ${}^e\mathbf{B}_i$. These parameters have been obtained from CAD modeling for ${}^e\mathbf{B}_i$ and from direct laser tracker measurements of the positions of the points $\mathbf{A}_i$.

Finally, estimations of the constant transformations ${}^m\mathbf{T}_e$ and ${}^f\mathbf{T}_b$ are needed. To this end, a laser tracker was used to accurately measured the CDPR mobile platform pose and, in order to make the calibration process easier, a few mobile platform poses with small rotations were considered.

5. Vision-Based Control Strategy

Visual servoing is based on the so-called interaction matrix $\mathbf{L_s}$ which relates the instantaneous relative Cartesian motion $\boldsymbol{\tau}$ between the mobile platform and the scene to the time derivative of a vector $\mathbf{s}$ [59]: $\dot{\mathbf{s}} = \mathbf{L_s}\boldsymbol{\tau}$. According to the definition of $\mathbf{s}$, several visual servoing techniques exist [28]: Image-based visual servoing, e.g. [27, 64], when $\mathbf{s}$ consists of features taken directly from the camera image, and position-based visual servoing, e.g. [65, 66], when $\mathbf{s}$ consists of 3D parameters which must be estimated from image measurements.

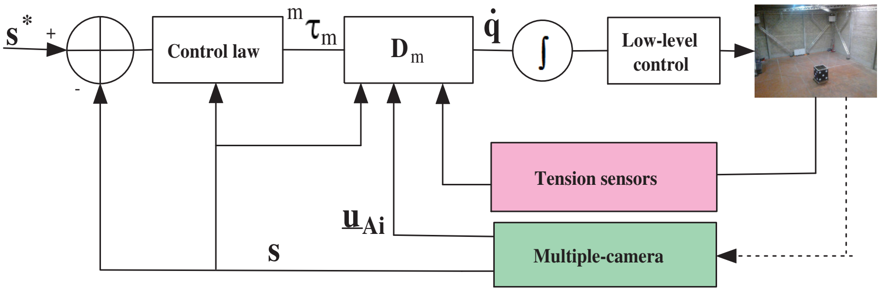

Figure 8: Vision Based Control (VBC) of the CDPR CoGiRo.

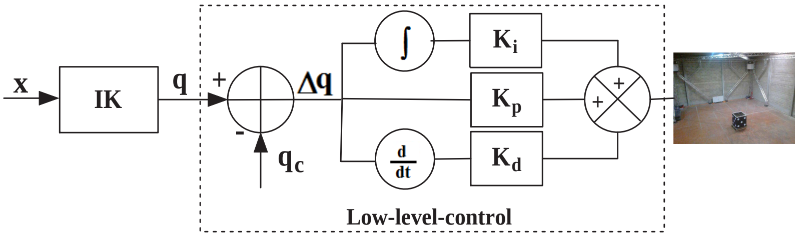

Figure 9: A classic Joint Space Control (JSC) applied to a CDPR. In the experiments on the CDPR CoGiRo, the values of the gains of the PID controller were $K_i = 57$ $[Nm/rad]$, $K_p = 267$ $[Nm/rad]$, and $K_d = 2.7$ $[Nm/rad]$ for each motor.

As the instantaneous inverse kinematics model (14) depends on the platform pose, we choose position-based visual servoing in the 3D pose form [65–67]: $\mathbf{s} = (\ \mathbf{s}_t \quad \mathbf{s}_w\ )^T$ and $\boldsymbol{\tau} = {}^m\boldsymbol{\tau}_m = {}^m\boldsymbol{\tau}_{m/m^*} = {}^m\boldsymbol{\tau}_{m/f}$, where, as defined previously in Section 3, ${}^j\boldsymbol{\tau}_i$ is the Cartesian velocity (linear and angular velocities) of $\mathcal{F}_i$ expressed in and with respect to $\mathcal{F}_j$. Let us consider $\mathcal{F}_m$ and $\mathcal{F}_{m^*}$ the current and the desired mobile frame locations, respectively. $\mathbf{s}_t = {}^m\mathbf{t}_{m^*}$ is the position error between $\mathcal{F}_m$ and $\mathcal{F}_{m^*}$ and $\mathbf{s}_w = \underline{\mathbf{u}}\theta$, where $\underline{\mathbf{u}}$ is the axis and θ is the angle of the rotation matrix ${}^m\mathcal{R}_{m^*}$ (angle-axis representation of ${}^m\mathcal{R}_{m^*}$).

Let us note that only information from the vision sensors is used to define the well-known interaction matrix $\mathbf{L}_\mathbf{s}$ given in [67, 68], using ${}^m\mathbf{T}_{m^*} = {}^m\mathbf{T}_f{}^f\mathbf{T}_{m^*}$.

To regulate the error between the current primitive vector $\mathbf{s}$ and the desired one $\mathbf{s}^* = \mathbf{0}$, the exponential decay $\dot{\mathbf{s}} = -\lambda\mathbf{s}$ is usually considered. The relationship between $\mathbf{s}$ and the end-effector Cartesian velocity ${}^m\boldsymbol{\tau}_m$ is then given by:

$$ {}^m\boldsymbol{\tau}_m = -\lambda\mathbf{L}_\mathbf{s}^{-1}\mathbf{s} \tag{18} $$

With ${}^f\boldsymbol{\tau}_e = \mathbf{D}_t{}^m\boldsymbol{\tau}_m$ and introducing (18) in (14) the vision-based control (Fig. 8) can be expressed as:

$$ \dot{\mathbf{q}} = \mathbf{D}_m{}^m\boldsymbol{\tau}_m = -\lambda\mathbf{D}_m\mathbf{L}_\mathbf{s}^{-1}\mathbf{s} \tag{19} $$

where $\mathbf{D}_m = \frac{1}{r_c}\mathbf{D}_a\mathbf{D}_t$, $\mathbf{D}_t = \begin{pmatrix} {}^f\mathbf{R}_m & {}^f\mathbf{R}_m[{}^m\overrightarrow{\mathbf{EM}}]_\times \\ \mathbf{0}_3 & {}^f\mathbf{R}_m \end{pmatrix}$ and point $\mathbf{M}$ is the origin of frame $\mathcal{F}_m$. Note that the choice of the cable model used in this vision-based control comes from matrix $\mathbf{D}_a$ which depends on the matrices $\mathbf{N}_i$, the latter being dependent on the cable model according to (11) and Tab. 3.

In the proposed Vision Based Control (VBC), the motor angular velocities $\dot{\mathbf{q}}$ are integrated to obtain the desired motor angles $\mathbf{q}$ which are the inputs to the low-level control scheme used in Fig. 8 and detailed in Fig. 9.

It shall be noted that cable tension measurements are notably affected by noise and cable vibrations. However, it is not a critical issue in the present work. Indeed, as can be seen in Fig. 8, these measurements are used to compute the current value of matrix $\mathbf{D}_m$ but are not involved in the feedback loop to compute the current tracking error. Indeed, the feedback loop is closed by means of vector $\mathbf{s}$ which is obtained from the vision-based measurement of the platform pose. However, filtering of the cable tensions measurements was essential to avoid unacceptable excessive values and sudden variations of the cable tension signals. It was

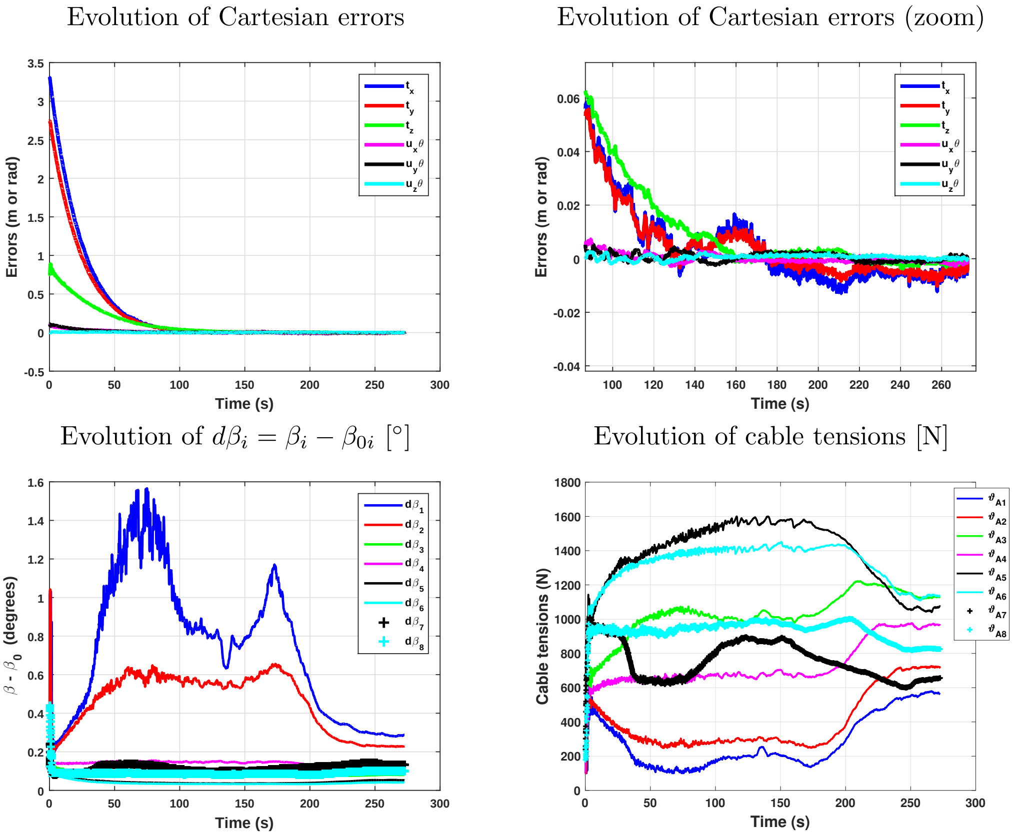
Evolution of Cartesian errors

Evolution of Cartesian errors (zoom)

Evolution of $d\beta_i = \beta_i - \beta_{0i}$ [°]

Evolution of cable tensions [N]

Figure 10: Vision based control of the CDPR CoGiRo using the SCMWE (Test 1).

also noted in Section 4.2 that the presence of friction causes a difference between the measured winch-level cable tensions and the actual cable tensions ϑ_{Ai} but this difference was not an issue in the experiments on the CDPR CoGiRo reported in the next section.

6. Experimental Results

The experimental results presented in this section concern the Simplified Catenary Model Without Elasticity (SCMWE) and the corresponding VBC strategy. Hence, this VBC does not require the cable longitudinal elasticity to be estimated which is an advantage because of the difficulty of accurately modeling cable elasticity.

For comparison purposes, the classic Joint Space Control (JSC) scheme shown in Fig. 9 is considered. It uses the aforementioned low-level control which consists of a PID controller with gains K_i, K_p and K_d. The measured motor angles $\mathbf{q}_c$ are compared to the desired ones $\mathbf{q}$ which are obtained from the desired mobile platform pose $\mathbf{x}$ by means of the inverse kinematics (IK) (Eq. (8)).

6.1. *Comparison of joint space and vision based control (JSC versus VBC)*

To evaluate the proposed approach, the robot CoGiRo is controlled to move a pallet weighing 110 kg—the total mass of the mobile platform (50 kg), the forklift (50 kg) and the pallet is 210 kg. The initial pose, shown in Fig. 2, consists of an initial mobile platform position ${}^f\mathbf{t}_m = (-0.09, -2.08, 9.22)^T$ [m] and an initial orientation given by ${}^f\underline{\mathbf{u}}\theta_m = (2.14, -1.03, 0.48)^T$ [rad] (angle-axis representation). In a first experiment (Test 1), the final pose consists of the position ${}^f\mathbf{t}_{m^*} = (-0.23, -5.56, 11.83)^T$ [m] and the

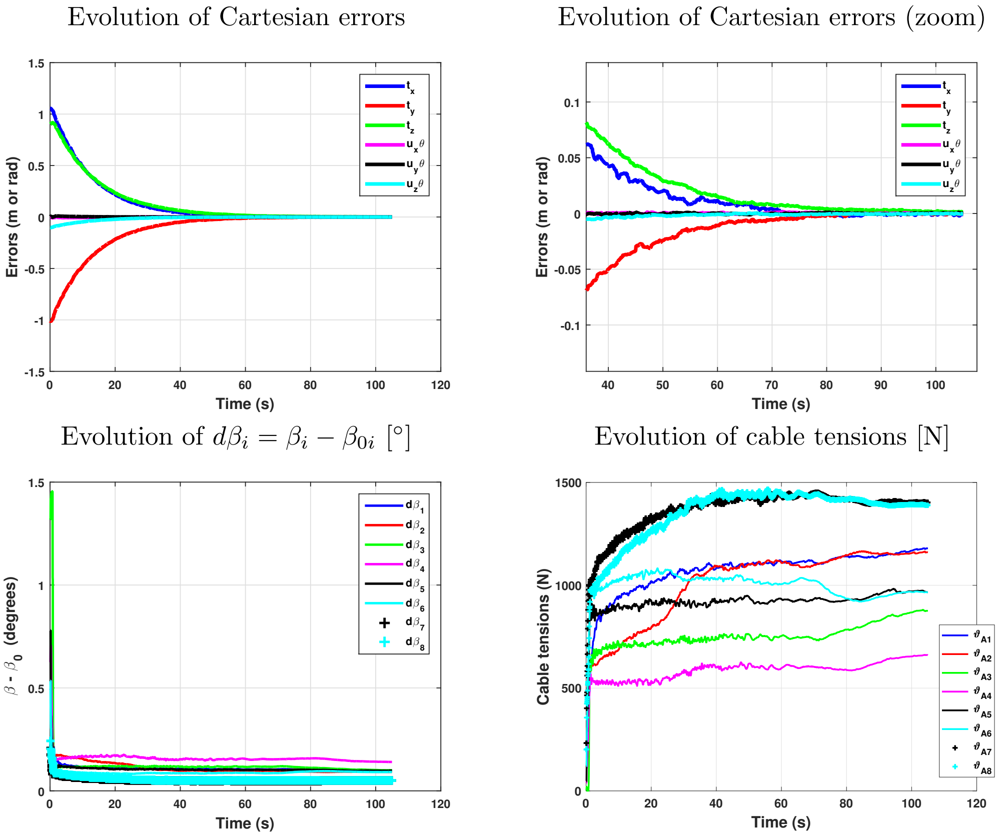

Evolution of Cartesian errors

Evolution of Cartesian errors (zoom)

Evolution of $d\beta_i = \beta_i - \beta_{0i}$ [°]

Evolution of cable tensions [N]

Figure 11: Vision based control of the CDPR CoGiRo using the SCMWE (Test 2).

orientation ${}^f\underline{\mathbf{u}}\theta_{m^*} = (2.15, -0.97, 0.65)^T$ [rad], while in a second experiment (Test 2), the final pose is given by ${}^f\mathbf{t}_{m^*} = (1.38, -2.86, 8.79)^T$ [m] and ${}^f\underline{\mathbf{u}}\theta_{m^*} = (2.18, -0.91, 0.44)^T$ [rad]. The trajectory followed by the moving platform of CoGiRo has motion amplitudes of 4.35 m and 8.0° in Test 1 and 1.72 m and 5.9° in Test 2. The angular amplitude is calculated as the angle of the angle-axis representation of the rotation matrix defining the orientation of the final pose with respect to the initial pose.

The results of these two experiments are presented in Fig. 10 and Fig. 11 where the VBC of Fig. 8 was used. This VBC was implemented with the SCMWE cable model. These figures show that the errors converge from initial Cartesian errors to steady state ones. Fig. 10 and Fig. 11 also show the filtered measurements of the cable tensions and of the angle differentials $d\beta_i = \beta_i - \beta_{0i}$, where the angles β_i and β_{0i} are defined in Fig. 4. The angle differentials $d\beta_i$ are small but not equal to zero which confirms that the cables are subjected to a (little) sagging. Moreover, the correspondence between the $d\beta_i$ and the cable tensions ϑ_{Ai} is consistent as can be clearly seen in Fig. 10 where the tensions in cables 1 and 2 is lower than the others and consequently $d\beta_1$ and $d\beta_2$ are larger. In the evolution of the cable tensions shown in this figure, it can be noticed that the cable tension distribution changes at the end of the trajectory when the mobile platform practically reached its final pose (approximately, at time 200 s). Explaining this change of tension distribution would require further investigation. Note that it did not happen in Test 2 (Fig. 11). In both Test 1 and Test 2, the cable tensions are small at the very beginning of the trajectory because the forklift attached to the mobile platform initially touches the ground.

The final pose reached by the mobile platform is measured by means of a laser tracker[3] and compared

---

[3] API Tracker3$^{\mathrm{TM}}$ having an angular resolution of ± 0.018 arc seconds, angular accuracy of 3.5 μm/meter and resolution of

	Translation errors [mm] $\begin{pmatrix} x & y & z \end{pmatrix}$	Orientation errors [°] $\begin{pmatrix} \phi & \theta & \psi \end{pmatrix}$
VBC: Test 1	$\begin{pmatrix} -1.0 & -9.9 & 5.7 \end{pmatrix}$	$\begin{pmatrix} -0.38 & -0.23 & 0.19 \end{pmatrix}$
VBC: Test 2	$\begin{pmatrix} 3.5 & 4.3 & -2.4 \end{pmatrix}$	$\begin{pmatrix} -0.08 & 0.06 & -0.05 \end{pmatrix}$
VBC: Test 3	$\begin{pmatrix} 0.1 & 4.2 & 2.7 \end{pmatrix}$	$\begin{pmatrix} 0.01 & 0.08 & 0.18 \end{pmatrix}$
JSC: Test 1	$\begin{pmatrix} 7.5 & -7.8 & -42.1 \end{pmatrix}$	$\begin{pmatrix} -0.65 & 10.73^{*} & -0.06 \end{pmatrix}$
JSC: Test 2	$\begin{pmatrix} 4.5 & 8.2 & -39.6 \end{pmatrix}$	$\begin{pmatrix} 0.28 & -0.23 & -0.36 \end{pmatrix}$
JSC: Test 3	$\begin{pmatrix} 2.76 & 1.4 & -31.6 \end{pmatrix}$	$\begin{pmatrix} 0.17 & 0.23 & 0.08 \end{pmatrix}$

Table 4: Position and orientation errors for Tests 1, 2 and 3 measured with a laser tracker: VBC vs JSC (in frame $\mathcal{F}_b$ and with X-Y-Z Euler angle convention); *: This value is an outlier which may be due to an error in the laser tracker measurement data.

to the desired one in order to determine the position and orientation errors. In Tab. 4, the errors obtained with the VBC are compared to the ones obtained by using only the simple JSC of Fig. 9. In the case of VBC, the accuracy results given in Tab. 4 are deemed very satisfactory for such a large-dimension CDPR. As expected, VBC ensures a better accuracy than JSC. Analyzing in more detail the results given in Tab. 4, the maximum error is seen to be -9.9 mm in position and -0.38° in orientation in the case of VBC. These maximum errors are much larger in the case of JSC, up to -42.1 mm for the position error.

Indeed, in the experiment, a heavy payload was attached to the mobile platform and then lifted. In such a situation, the cable elongations are not negligible. In the case of JSC, the cable lengths are indirectly used for regulation but the cable elongations have not been taken into account because of the difficulty of modeling them accurately. Consequently, the positioning accuracy along the vertical axis $\underline{\mathbf{z}}_b$ is relatively poor as illustrated in Tab. 4. In the case of VBC, as it can be expected, even if the cable elongations are not included in the modeling (the cable elasticity is disregarded in the SCMWE cable model), the positioning accuracy is improved since the mobile platform pose is measured and used for regulation, with a significant improvement along the vertical axis $\underline{\mathbf{z}}_b$. A third experiment (Test 3) was made without the 110 kg payload so that only the mobile platform and forklift mass (net mass of 100 kg) is suspended on the cables of the CDPR CoGiRo. The initial pose is given by ${}^f\mathbf{t}_m = (-0.084, -2.07, 9.21)^T$ [m], ${}^f\underline{\mathbf{u}}\,\theta_m = (2.14, -1.04, 0.49)^T$ [rad], and the final pose by ${}^f\mathbf{t}_{m^*} = (-0.05, -2.79, 8.52)^T$ [m], ${}^f\underline{\mathbf{u}}\theta_{m^*} = (2.22, -0.75, 0.37)^T$ [rad], which corresponds to motion amplitudes of 1.0 m and 14.5°. The mass suspended on the cables being smaller than the one in Test 1 and Test 2, the cable tensions are also smaller as shown in Fig. 12. The position and orientation errors for Test 3 are given in Tab. 4. It is apparent that the JSC error along the vertical axis $\underline{\mathbf{z}}_b$ obtained in Test 3 (-31.6 mm) is lower than the ones in Tests 1 and 2, which is a direct consequence of the fact that a smaller mass is suspended on the cables. Moreover, similarly to Tests 1 and 2, VBC leads to a globally better accuracy than JSC. It can also be noted from this table that VBC is not sensitive to the carried mass, contrary to JSC where errors in Test 3 (mass of 100 kg) are on overall smaller than those in Tests 1 and 2 (mass of 210 kg).

6.2. Comparison of a sagging and a non-sagging cable model

The goal of this subsection is to compare the results obtained with VBC in two cases. In the first case, as in Section 6.1, the SCMWE sagging cable model is used whereas, in the second case, the non-sagging Straight-Line Segment Model (SLSM) is used so that the cable mass is not accounted for. These two cases are compared by means of two experiments on the CDPR CoGiRo where only the mobile platform and forklift mass (100 kg) is suspended on the cables. In both experiments, the initial mobile platform pose consists of the position ${}^f\mathbf{t}_m = (0.07, -1.04, 8.9)^T$ [m] and the orientation ${}^f\underline{\mathbf{u}}\theta_m = (2.17, -1.06, 0.48)^T$ [rad]. In one experiment (Test 4), the mobile platform is controlled to reach the final pose ${}^f\mathbf{t}_{m^*} = (-0.7, -1.79, 7.49)^T$

0.1μm. These specifications yield a very high precision when measurements are made at some meters from the tracker which is the case in these experiments. According to our experience, the actual precision in measuring a 3D point can be considered to be less than 0.1 mm.

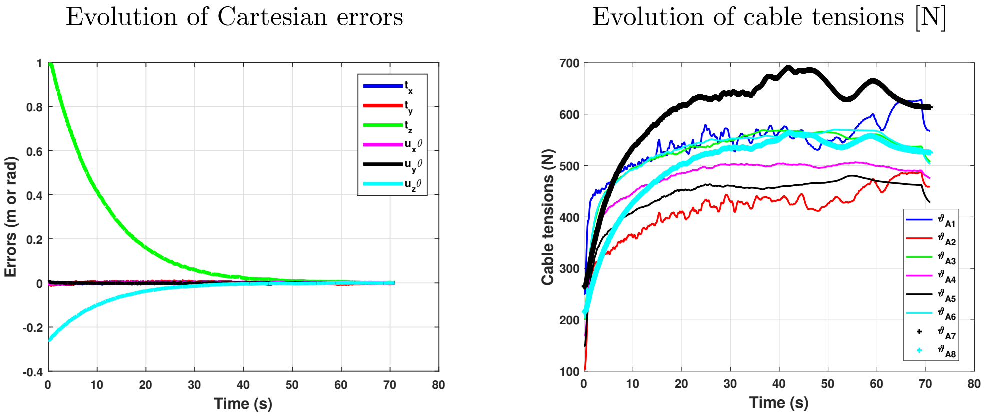

Figure 12: Vision based control of the CDPR CoGiRo using the SCMWE (Test 3, without the pallet of 110 kg).

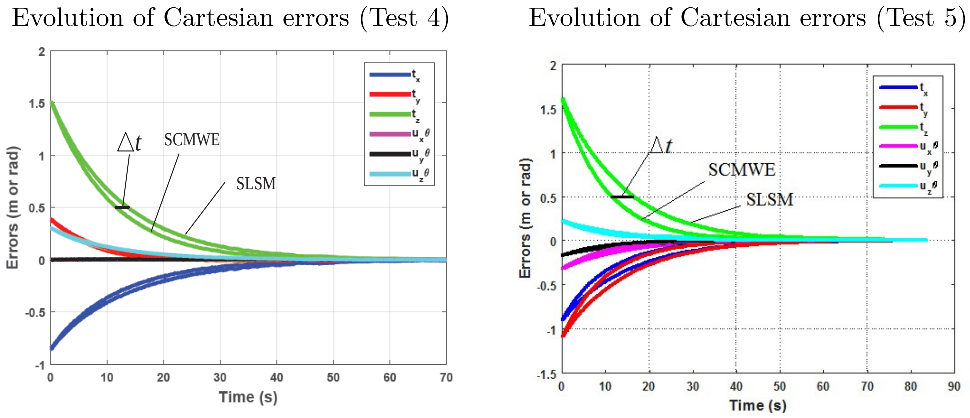

Figure 13: Evolution of Cartesian errors: Comparison of VBC using either the SCMWE or the SLSM in two experiments (Tests 4 and 5).

[m] and ${}^{f}\underline{\mathbf{u}}\theta_{m^*} = (2.02, -1.39, 0.61)^T$ [rad], while in the second experiment (Test 5), the final pose is ${}^{f}\mathbf{t}_{m^*} = (0.44, -1.17, 6.81)^T$ [m] and ${}^{f}\underline{\mathbf{u}}\theta_{m^*} = (1.85, -1.38, 0.2)^T$ [rad]. The trajectory followed by the moving platform has motion amplitudes of 1.77 m and 16.9° in Test 4 and 2.12 m and 24.3° in Test 5.

Fig. 13 shows the evolution of the Cartesian errors obtained with VBC using the SCMWE and with VBC using the SLSM. In the latter case, the cables are tensed and considered massless and inextensible. Thereby, the instantaneous inverse kinematics model depends only on the pose of the mobile platform and on some constant (calibration) parameters [25]. As shown in Fig. 13, in both model cases and in both experiments, the Cartesian errors converge exponentially to a final values close to zero. It reflects the property of the VBC where the moving platform pose is measured.

However, two different convergence times can be distinguished. As shown in Fig. 13, using SCMWE in VBC leads to a faster convergence time than VBC with SLSM. The most significant value of all six convergence times is on the t_z value (green curves in Fig. 13). As indicated in Tab. 5, the corresponding time difference $\triangle t$ between the SCMWE and the SLSM is approximately equal to 1.7 s in Test 4 and to 4.96 s in Test 5. Tab. 5 also shows the mean values of the final error vector norm. These accuracy results are deemed very satisfactory for the proposed VBC based on the SCMWE since a position error of a few millimeters is obtained.

The experiments were performed using 50 Frames Per Second (FPS), 1280 x 1024, GigE cameras, which

	Mean position error [mm]	Mean orientation error [°]	$\triangle t$ (s)
SCMWE: real robot (Test 4)	2.1	0.01	-1.72
SLSM: real robot (Test 4)	7.61	0.04	
SCMWE: real robot (Test 5)	4.48	0.08	-4.96
SLSM: real robot (Test 5)	6.55	0.09	
SCMWE: simulator (Test 4)	3.5	0.02	-1.05
SLSM: simulator (Test 4)	4.9	0.02	

Table 5: Comparison of VBC using SCMWE and VBC using SLSM: Mean values of final Cartesian errors and time differences (Tests 4 and 5).

were sufficient to prove the validity, in quasi-static CDPR operation, of the VBC approach proposed in this paper, which performs at a 20 Hz sampling frequency. While being out of the scope of this paper, let us note that cameras with higher FPS may be used to help achieving a high-speed VBC, as for instance in [32, 69], and thus to increase the feasible velocities and accelerations of the CDPR mobile platform. It would also require an optimization of the time needed for VBC calculations and for processing of all camera raw images, which took 0.04 s on average on a desktop PC equipped with an Intel Core i7 processor, 16 GB RAM, and a GPU GeForce GTX 550 Ti.

6.3. The influence of the calibration method

The calibration method in 4.3 used to estimate the constant parameters and transformations is an approximate method. However, it was satisfactory enough for the proposed VBC. In fact, the implemented 3D pose control law depends only on the pose of the mobile platform, which is robust to significant calibration errors. We can evaluate the calibration in view of the results shown in Figs. 10, 11 and 13. In all cases, the Cartesian errors converge exponentially to a small final errors. If significant calibration errors were made, overshoots and significant steady-state errors would appear, which could be reduced by a more careful calibration [70].

7. Simulation Results

7.1. Cable sagging in the experiments

Fig. 10 shows the measurements of the angle differentials $d\beta_i = \beta_i - \beta_{0i}$, the angles β_i and β_{0i} being defined in Fig. 4. $d\beta_i$ is not equal to zero which confirms that the cable profiles are not straight lines segments (sagging). However, the values of $d\beta_i$ are generally small meaning that the cable sagging is relatively small. This limited sagging in turn justifies the use of the SCMWE in the experiments reported in Section 6. Nevertheless, the small values of $d\beta_i$ also indicate that the CDPR CoGiRo and/or the diameters of its cables may not be large enough for the cable mass to have a significant influence.

In fact, as it can be expected, considering three scaled versions of the robot CoGiRo, the angle differentials $d\beta_i = \beta_i - \beta_{0i}$ computed for a given mobile platform pose increase with the dimensions of the robot as presented in the results given in Tab. 6.

\ l x w x h	16.2 x 22.2 x 8.3 [m]	27 x 37 x 13.9 [m]	75 x 98 x 38.9 [m]
$d\beta_1$	1.3	2.5	5.7
$d\beta_2$	1.3	2.5	5.4
$d\beta_3$	3.2	5.3	8.3
$d\beta_4$	1.5	2.6	5.5
$d\beta_5$	0.8	1.6	4.2
$d\beta_6$	3.15	6.2	9.4
$d\beta_7$	1.8	3.3	6.3
$d\beta_8$	2.2	3.4	6.9

Table 6: For a given pose of the mobile platform, values of $d\beta_i = \beta_i - \beta_{0i}$ [°] obtained for three scaled versions of the CDPR CoGiRo (the scaled dimensions are length x width x height) and computed by means of the SCMWE.

Consequently, while the experimental results presented in Section 6 show the feasibility and interests of the proposed VBC strategy, the latter may be more relevant for CDPRs larger than CoGiRo or using cables with larger diameters. The latter situation should be the case in many industrial applications where factors of safety have to be used in the design of a CDPR and hence in selecting its cables.

7.2. Comparison of models in simulations

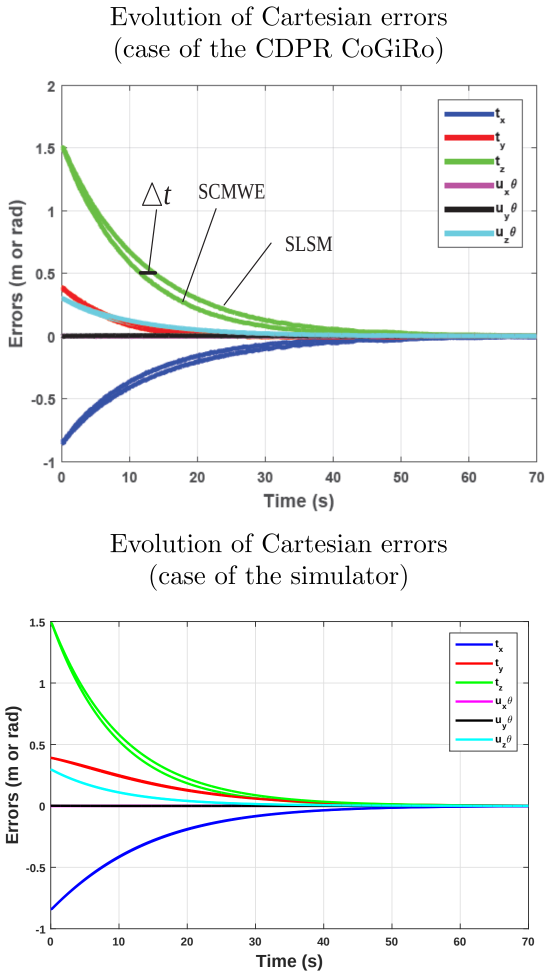

Figure 14: Evolution of Cartesian errors along the trajectory of Test 4: Qualitative comparison of the experimental results on the real robot (CDPR CoGiRo) and the results obtained with the simulator.

As pointed out above, the CDPR CoGiRo may not be large enough to further assess the relevance of the proposed VBC strategy. Hence, since no larger CDPR was available to further test the proposed VBC, a comparison of cable models used in VBC has been done with a simulator of large-dimension CDPRs. In brief, the CDPR is simulated based on kinematics and dynamics models. The equations of motions are implemented by means of Newton-Euler equations of the 6-DOF CDPR mobile platform and of the winches, using appropriately scaled values of the geometric and dynamics parameters of the CDPR CoGiRo. Moreover, the directions of the forces applied by the cables on the mobile platform are computed with (4). Hence, the cable dynamics is neglected but the cable sagging is accounted for (substituting static cable forces at a given mobile platform pose for dynamic cable forces), which is consistent with the quasi-static CDPR operation assumed in this paper. In this simulator, the camera and cable tension measurements are assumed to be perfect and the simulated CDPR is controlled by means of the VBC proposed in this paper.

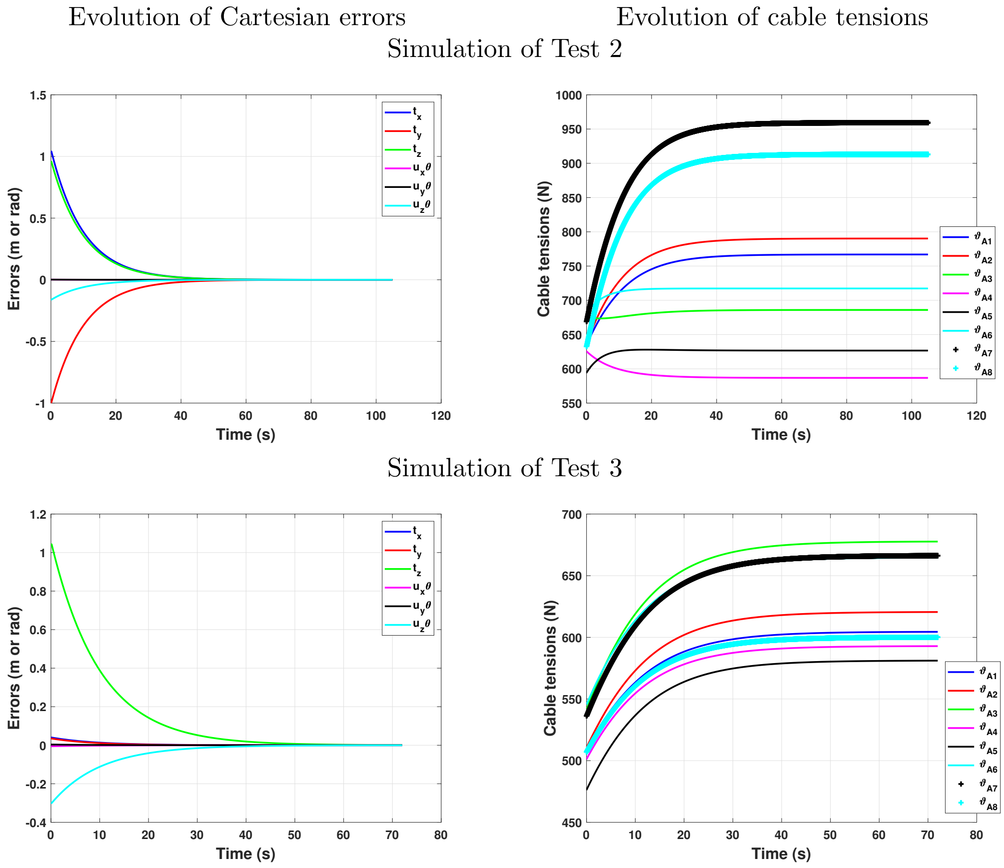

Evolution of Cartesian errors

Evolution of cable tensions

Simulation of Test 2

Simulation of Test 3

Figure 15: Results of the simulations of Tests 2 and 3 of Section 6.1.

First, the CDPR CoGiRo following the trajectories of Test 4 presented in Section 6.2, where VBC using the SCMWE is compared to VBC using the SLSM, is simulated. The results of these simulations are shown in Fig. 14 and Tab. 5. As can be seen in Fig. 14, where the evolution of the Cartesian errors can be compared, the CDPR mobile platform trajectory produced by the simulator corresponds well to the experiments. Additionally, the results of the simulations of Tests 2 and 3 are shown in Fig. 15. Comparing this figure with Fig. 11 and Fig. 12, it can be seen that the Cartesian errors are very similar confirming the ability of the simulator to reproduce the Cartesian trajectory followed by the mobile platform. However, the cable tensions curves are relatively different. Besides the absence of noise in the simulated cable tension signals, the cable tension values are on overall larger in the experiments than in simulation which can be mainly attributed to the significant friction acting at the winches and at the cable drawing points where eyelets were used. Moreover, even if cables 1, 2, 7 and 8 are seen to be the most tensed in Test 2 both in simulation and in experiment, the cable tension distributions in the simulations are not the same as those in the experiments. These differences in cable tension distributions are not surprising since friction is not included in the simulations and several cable tension distributions are possible in a given pose and along a trajectory [71]. In the simulator, only one tension distribution is calculated by means of a pseudo-inverse (see in Appendix A.2 and in [56]). Hence, realistic simulation of the cable tensions would require significant further work and is out of the scope of the present paper. Nevertheless, being given the similarities between the trajectories followed by the mobile platform in experiments and in simulations, the simulator can be used to get some insight into the application of the proposed vision-based modeling and control to CDPRs of larger dimensions.

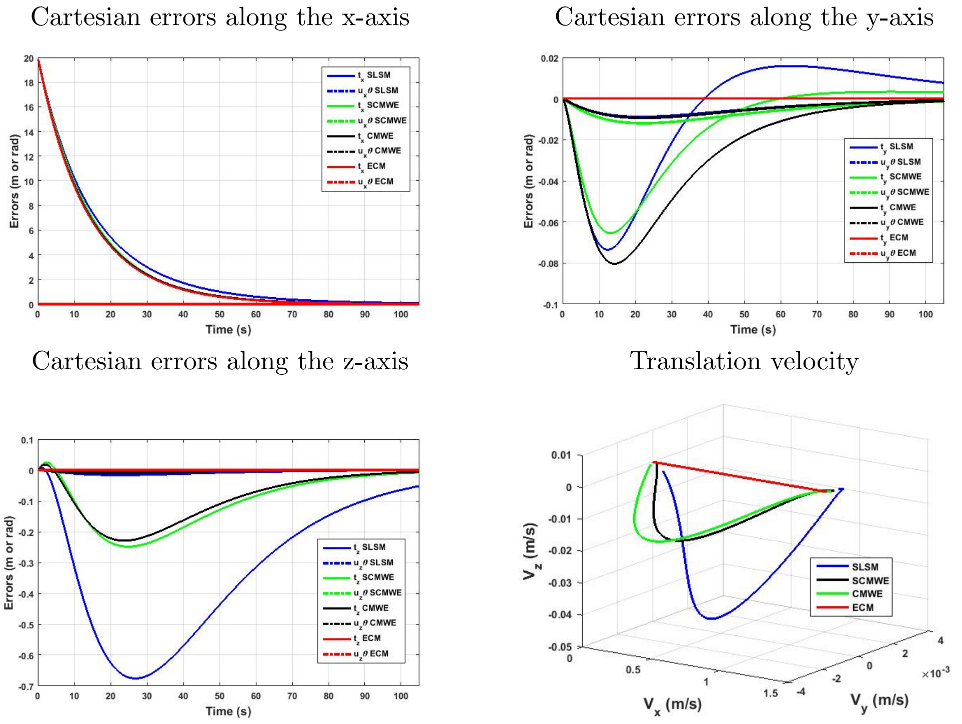

Figure 16: Evolution of Cartesian errors and linear velocities (simulation results in the case of ECM, CMWE, SCMWE and SLSM models).

	Mean position error [mm]	Mean orientation error [°]	$\triangle t$ [s] compared to SLSM
ECM	13.03	0.16	-2.25
CMWE	18.84	0.20	-1.95
SCMWE	24.22	0.24	-1.59
SLSM	87.63	0.72	

Table 7: Final Cartesian errors: Means of the position and orientation errors along the x, y and z axis.

Then, a very large CDPR of dimensions 75 m x 98 m x 38.9 m (l x w x h) is simulated by appropriately scaling the dimensional parameters of the CDPR CoGiRo. In these simulations, a comparison of the proposed VBC strategy, when using four different cable models (ECM, CMWE, SCMWE and SLSM) has been made. The ECM consists in using Eq. (6) and (11) with a fourth order series expansion ($O_l = 4$). In the simulations, the VBC is used to make the mobile platform move from the initial pose ${}^b\mathbf{E} = (0, 0, 0)^T$ [m] and $(\theta_x, \theta_y, \theta_z)^T = (0, 0, 0)^T$ [°] to the final pose ${}^b\mathbf{E}^* = (20, 0, 0)^T$ [m] and $(\theta_x^*, \theta_y^*, \theta_z^*)^T = (0, 0, 0)^T$ [°] (X-Y-Z Euler angles convention).

The simulation results are shown in Fig. 16, where the simulation was stopped at 105 s. As expected, the Cartesian errors converge exponentially to small final errors. In the case of the VBC using the CMWE, SCMWE or ECM, compared to that of SLSM, a significantly faster convergence time can be observed (Fig. 16 and Tab. 7). The best positioning accuracy results (Tab. 7) are obtained with the VBC based on the ECM.

Besides, as shown in Fig. 16, the Cartesian errors using the CMWE, SCMWE and SLSM have overshoots in some curves showing that the ECM should be more appropriate for large-dimension CDPRs than the other models (CMWE, SCMWE, SLSM). Especially in the case of SLSM, due to (simulated) modeling and calibration errors, the instantaneous inverse kinematics associated with the motor angular velocities does not allow, initially, to orient the robot mobile platform in the desired direction. Consequently, overshoots appear in some Cartesian error and velocity curves (Fig. 16). These overshoots are however gradually reduced thanks to the VBC which is known to be robust to significant modeling errors [67, 72].

8. Conclusion

This paper introduced instantaneous inverse kinematics models and a vision-based control strategy for large-dimension CDPRs displacing heavy payloads in quasi-static operation. The instantaneous inverse kinematics models have been obtained from an original formulation of the inverse kinematics based on the elastic catenary cable model. These models dependent on the mobile platform pose, the cable tangent directions, and the cable tensions. In order to obtain the corresponding measurements, a multi-camera setup in an eye-to-hand configuration has been used together with force sensors. Based on this modeling and measurement means, a position-based visual servo control has been implemented, where the mobile platform pose is measured by vision and used for regulation. This vision-based control has been validated experimentally on the large-dimension CDPR CoGiRo allowing its mobile platform to be accurately positioned without having to estimate the cable elastic characteristics.

The experiments reported in this paper were mainly based on the proposed vision-based control implemented with a non-negligible mass cable model. In the latter, the cable sag is assumed to be relatively small. This assumption proved to be valid in the reported experiments on the CDPR CoGiRo but its validity may be a concern in the case of larger CDPRs, or for CDPRs actuated by cables of larger diameters. Consequently, the proposed vision-based control, implemented by means of four different instantaneous inverse kinematics models, has been applied in simulation to a CDPR significantly larger than the robot CoGiRo. The results of these simulations indicate that for very large CDPRs vision-based control may be reinforced by an accurate sagging cable model to avoid possible overshoots and improve convergence time, which needs to be confronted to real-life experiments.

9. Acknowledgments

This work was supported by the ANR (grant 2009 SEGI 018, CoGiRo project).

Appendix A. Interaction Matrix Expressions

The detailed derivation of the interaction matrices $\mathbf{D}_{Bi}$ and $\mathbf{D}_{si}$ introduced in Section 3 can be found in our previous work [56]. In this appendix, the expressions of $\mathbf{D}_{Bi}$ and $\mathbf{D}_{si}$ are recalled for completeness.

Appendix A.1. Expressions of matrix $\mathbf{D}_{Bi}$

Matrix $\mathbf{D}_{Bi}$ used in (12) is defined as follows:

$$\mathbf{D}_{Bi} = {}^{Ai}\mathbf{R}_f \left([{}^f\overrightarrow{\mathbf{A}_i\mathbf{B}_i}]_\times \mathbf{D}_{\gamma_i} + \mathbf{D}_{Bfi} \right)$$

where ${}^{Ai}\mathbf{R}_f$ is the rotation matrix defining the orientation of $\mathcal{F}_f$ in $\mathcal{F}_{Ai}$, and $[{}^f\overrightarrow{\mathbf{A}_i\mathbf{B}_i}]_\times$ is the cross-product matrix associated with vector $\overrightarrow{\mathbf{A}_i\mathbf{B}_i}$. Moreover, the matrices $\mathbf{D}_{Bfi}$ and $\mathbf{D}_{\gamma_i}$ are defined as:

- $\mathbf{D}_{Bfi} = \left(\mathbf{I}_3,\ -[{}^f\mathbf{R}_e{}^e\mathbf{B}_i]_\times\right)$ where $\mathbf{I}_3$ is the 3×3 identity matrix, ${}^f\mathbf{R}_e$ the rotation matrix defining the orientation of $\mathcal{F}_e$ in $\mathcal{F}_f$ and ${}^e\mathbf{B}_i$ the position vector of point $\mathbf{B}_i$ in $\mathcal{F}_e$
- $\mathbf{D}_{\gamma_i} = {}^f\underline{\mathbf{z}}_{Ai}\mathbf{D}_{0i}{}^b\mathbf{R}_f\mathbf{D}_{ui}$ where $\mathbf{D}_{0i} = \frac{1}{{}^bu_{ix}^2 + {}^bu_{iy}^2}\left(-{}^bu_{iy}, {}^bu_{ix}, 0\right)$,

  $\mathbf{D}_{ui} = \frac{1}{L_i}(\mathbf{I}_3 - {}^f\underline{\mathbf{u}}_i{}^f\underline{\mathbf{u}}_i^T)\mathbf{D}_{Bfi}$, the vectors $\underline{\mathbf{z}}_{Ai}$ and ${}^b\underline{\mathbf{u}}_i = \left({}^bu_{ix}, {}^bu_{iy}, {}^bu_{iz}\right)^T$ are defined in Section 2, ${}^f\underline{\mathbf{u}}_i ={}^f \mathbf{R}_b{}^b\underline{\mathbf{u}}_i$, and $L_i = \| \overrightarrow{\mathbf{A}_i\mathbf{B}_i} \|$ is the length of the straight line segment between $\mathbf{A}_i$ and $\mathbf{B}_i$.

Appendix A.2. Expressions of matrix $\mathbf{D}_{si}$

Matrix $\mathbf{D}_{si}$ used in (12) is the ith row of the matrix $\mathbf{D}_s = -\mathbf{D}_\vartheta^+ \sum_{i=1}^{k} \mathbf{D}_{\tau_i}$ where $\mathbf{D}_\vartheta^+$ is the pseudo-inverse of $\mathbf{D}_\vartheta = (\mathbf{D}_{\vartheta_1}, ..., \mathbf{D}_{\vartheta_k})$ with:

$$\mathbf{D}_{\vartheta_i} = \begin{pmatrix} \mathbf{D}_{ui2} \\ [{}^f\overrightarrow{\mathbf{EB}_i}]_\times \mathbf{D}_{ui2} \end{pmatrix}$$

and

$$\mathbf{D}_{\tau_i} = \begin{pmatrix} \mathbf{D}_{u\rho_i} + \mathbf{D}_{ui1} \\ -[{}^f\mathbf{u}_{Bi}]_\times \mathbf{D}_{EBi} + [{}^f\overrightarrow{\mathbf{EB}_i}]_\times (\mathbf{D}_{u\rho_i} + \mathbf{D}_{ui1}) \end{pmatrix}$$

$$\mathbf{D}_{ui1} = \left(\mathbf{D}_{fi}\mathbf{D}_{Bi} + \frac{{}^{Ai}\vartheta_{Bix}}{\cos(\beta_{0i})} \mathbf{D}_{ui} \right)$$

$$\mathbf{D}_{fi} = \frac{{}^{Ai}\vartheta_{Bix} \sin(\beta_{0i}) {}^f\underline{\mathbf{u}}_i}{{}^{Ai}B_{ix}^2} \begin{pmatrix} -{}^{Ai}B_{iz} & 0 & {}^{Ai}B_{ix} \end{pmatrix}$$

$$\mathbf{D}_{ui2} = \frac{{}^f\underline{\mathbf{u}}_i}{\cos(\beta_{0i})}, \quad \mathbf{D}_{EBi} = \begin{pmatrix} \mathbf{0}_3 & -[{}^f\mathbf{R}_e {}^e\mathbf{B}_i]_\times \end{pmatrix}$$

$$\mathbf{D}_{u\rho_i} = \frac{\rho_0 g}{2} {}^f\underline{\mathbf{z}}_{Ai} {}^f\underline{\mathbf{u}}_i^T \mathbf{D}_{Bfi}$$

where $\mathbf{D}_{Bi}$ and $\mathbf{D}_{Bfi}$ are defined in Appendix A.1.

Appendix B. About the Usage of ViSP to Estimate the Mobile Platform Pose

ViSP [63] provides several algorithms allowing to estimate the pose of the mobile platform of a CDPR pose from points. In this paper, the points are the white points forming the patterns attached to the mobile platform. Several approaches (Dementhon, Lagrange, Lowe, Ransac and virtual visual servoing (VVS)) are available in VISP to estimate the pose from points:

- Pose estimation from points is implemented in *vpPose::class*.
- To consider point features, one can use *vpPose::addPoint(const vpPoint)*
- The pose is computed using *vpPose::computePose()* function. At least four points are needed.

References

[1] J. Merlet, Parallel robots, Kluwer Academic Publishers, 2000.

[2] I. A. Bonev, The true Origins of Parallel Robots, ParalleMIC: the Parallel Mechanisms Information Center, 2003.

[3] R. G. Roberts, T. Graham, T. Lippitt, On the inverse kinematics, statics, and fault tolerance of cable-suspended robots, Journal of Robotic Systems 15 (1998) 581–597.

[4] S. Abdelaziz, L. Esteveny, L. Barbé, P. Renaud, B. Bayle, M. De Mathelin, Development of a MR-compatible cable-driven manipulator : Design and technological issues, in: IEEE International Conference on Robotics and Automation, ICRA, St Paul, Minnesota, 2012, pp. 1488–1494.

[5] K. Kozak, Q. Zhou, J. Wang, Static analysis of cable-driven manipulators with non-negligible cable mass, IEEE Transactions on Robotics 22 (3) (2006) 425–433.

[6] J. Albus, R. Bostelman, N. Dagalakis, The NIST robocrane, J. Robot. Syst. 10 (5) (1993) 709–724.

[7] R. L. Williams II, M. Xin, P. Bosscher, Contour-crafting-cartesian-cable robot system concepts: Workspace and stiffness comparisons, in: Proc. ASME Int. Design Engineering Technical Conf. and Computers and Information in Engineering Conf., no. DETC2008-49478, Brooklyn, NY, 2008.

[8] SKYCAM, http://www.skycam.tv/.

[9] M. Ishii, M. Sato, A 3D spatial interface device using tensed strings, Presence 3 (1) (1994) 81–86.

[10] L. Yingjie, Z. Wenbai, R. Gexue, Feedback control of a cable-driven gough-stewart platform, IEEE Transactions on Robotics 22 (1) (2006) 198–202.

[11] C. Lambert, M. Nahon, D. Chalmers, Implementation of an aerostat positioning system with cable control, IEEE/ASME Transactions on Mechatronics 12 (1) (2007) 32–40.

[12] A. Pott, Cable-Driven Parallel Robots, Theory and Application, Springer, 2018.

[13] V. Schmidt, Modeling techniques and reliable real-time implementation of kinematics for cable-driven parallel robots using polymer fiber cables, Ph.D. thesis, Fraunhofer Verlag, Stuttgart, Germany (2017).

[14] J.-B. Izard, A. Dubor, P.-E. Hervé, E. Cabay, D. Culla, M. Rodriguez, M. Barrado, On the improvements of a cable-driven parallel robot for achieving additive manufacturing for construction, in: C. Gosselin, P. Cardou, T. Bruckmann, A. Pott (Eds.), Cable-Driven Parallel Robots, Springer, 2017, pp. 353–363.

[15] S. Baklouti, S. Caro, E. Courteille, Sensitivity analysis of the elasto-geometrical model of cable-driven parallel robots, in: C. Gosselin, P. Cardou, T. Bruckmann, A. Pott (Eds.), Cable-Driven Parallel Robots, Springer, 2017, pp. 37–49.

[16] J. Piao, X. Jin, E. Choi, J.-O. Park, C.-S. Kim, J. Jung, A polymer cable creep modeling for a cable-driven parallel robot in a heavy payload application, in: C. Gosselin, P. Cardou, T. Bruckmann, A. Pott (Eds.), Cable-Driven Parallel Robots, Springer, 2017, pp. 62–72.

[17] A. Pott, An algorithm for real-time forward kinematics of cable-driven parallel robots, Advances in Robot Kinematics: Motion in Man and Machine (2010) 529–538.

[18] J.-P. Merlet, J. Sandretto, The forward kinematics of cable-driven parallel robots with sagging cables, in: T. Bruckmann, A. Pott (Eds.), Cable-Driven Parallel Robots, Springer, 2014, pp. 3–15.

[19] A. Berti, J.-P. Merlet, M. Carricato, Solving the direct geometrico-static problem of underconstrained cable-driven parallel robots by interval analysis, International Journal of Robotics Research 35 (6) (2016) 723–739.

[20] A. Aflakian, A. Safaryazdi, M. T. Masouleh, A. Kalhor, Experimental study on the kinematic control of a cable suspended parallel robot for object tracking purpose, Mechatronics 50 (2018) 160–176.

[21] R. L. Williams II, B. Snyder, J. S. Albus, R. V. Bostelman, Seven-DOF cable-suspended robot with independent metrology, in: Proc. ASME Design Engineering Technical Conf. and Computers and Information in Engineering Conf., no. DETC2004/MECH-57125, Salt Lake City, UT, 2004.

[22] X. Garant, A. Campeau-Lecours, P. Cardou, C. Gosselin, Improving the forward kinematics of cable-driven parallel robots through cable angle sensors, in: C. Gosselin, P. Cardou, T. Bruckmann, A. Pott (Eds.), Cable-Driven Parallel Robots, Springer, 2017, pp. 167–179.

[23] J.-P. Merlet, Direct kinematics of CDPR with extra cable orientation sensors: The 2 and 3 cables case with perfect measurement and ideal or elastic cables, in: C. Gosselin, P. Cardou, T. Bruckmann, A. Pott (Eds.), Cable-Driven Parallel Robots, Springer, 2017, pp. 180–191.

[24] H. Kino, T. Yahiro, F. Takemura, T. Morizono, Robust PD control using adaptive compensation for completely restrained parallel-wire driven robots: Translational systems using the minimum number of wires under zero-gravity condition, IEEE Transactions on Robotics 23 (4) (2007) 803–812.

[25] T. Dallej, M. Gouttefarde, N. Andreff, M. Michelin, P. Martinet, Towards vision-based control of cable-driven parallel robots, in: IEEE International Conference on Intelligent Robots and Systems, IROS, San Francisco, California, 2011, pp. 2855–2860.

[26] L. Weiss, A. Sanderson, C. Neuman, Dynamic sensor-based control of robots with visual feedback, IEEE Transactions on Robotics and Automation 3 (5) (1987) 404–417.

[27] B. Espiau, F. Chaumette, P. Rives, A new approach to visual servoing in robotics, IEEE Transactions on Robotics and Automation 8 (3) (1992) 313–326.

[28] F. Chaumette, S. Hutchinson, Visual servo control part I: Basic approaches, IEEE Robotics and Automation Magazine 13 (4) (2006) 82–90.

[29] R. Chellal, L. Cuvillon, E. Laroche, A kinematic vision-based position control of a 6-DOF cable-driven parallel robot, in: Cable-Driven Parallel Robots, Springer, 2014, pp. 213–226.

[30] R. Babaghasabha, M. A. Khosravi, H. D. Taghirad, Adaptive robust control of fully-constrained cable driven parallel robots, Mechatronics 25 (2015) 27–36.

[31] M. H. Korayem, M. Taherifar, H. Tourajizadeh, Compensating the flexibility uncertainties of a cable suspended robot using SMC approach, Robotica 33 (3) (2015) 578–598.

[32] J. Begey, L. Cuvillon, M. Lesellier, M. Gouttefarde, J. Gangloff, Dynamic control of parallel robots driven by flexible cables and actuated by position-controlled winches, IEEE Trans. on Robotics (to appear).

[33] J.-D. Deschenes, P. Lambert, S. Perreault, N. Martel-Brisson, N. Zoso, A. Zaccarin, P. Hebert, S. Bouchard, C. Gosselin, A cable-driven parallel mechanism for capturing object appearance from multiple viewpoints, in: Sixth International Conference on 3-D Digital Imaging and Modeling, Montreal, Canada, 2007.

[34] R. Ramadour, F. Chaumette, J.-P. Merlet, Grasping objects with a cable-driven parallel robot designed for transfer operation by visual servoing, in: Proc. IEEE Int. Conf. Robotics and Automation (ICRA), Hong Kong, China, 2014, pp. 4463–4468.

[35] A. R. Emmens, S. Spanjer, J. L. Herder, Modeling and control of a large-span redundant surface constrained cable robot with a vision sensor on the platform, in: T. Bruckmann, A. Pott (Eds.), Cable-Driven Parallel Robots, Springer, 2014, pp. 249–260.

[36] S. Kawamura, H. Kino, C. Won, High-speed manipulation by using parallel wire-driven robots, Robotica 18 (2000) 13–21.

[37] A. B. Alp, S. K. Agrawal, Cable suspended robots: design, planning and control, in: IEEE International Conference on Robotics and Automation (ICRA), Washington, DC, USA, 2002, pp. 4275 – 4280.

[38] M. A. Khosravi, H. D. Taghirad, Robust PID control of fully-constrained cable driven parallel robots, Mechatronics 24 (2014) 87–97.

[39] M. A. Khosravi, H. D. Taghirad, Dynamic modeling and control of parallel robots with elastic cables: Singular perturbation approach, IEEE Trans. on Robotics 30 (3) (2014) 694–704.

[40] X. Weber, L. Cuvillon, J. Gangloff, Active vibration canceling of a cable-driven parallel robot in modal space, in: Proc.

IEEE Int. Conf. Robotics and Automation (ICRA), Seattle, Washington, 2015, pp. 1599–1604.

[41] H. Jamshidifar, S. Khosravani, B. Fidan, A. Khajepour, Kinematically-constrained redundant cable-driven parallel robots: Modeling, redundancy analysis, and stiffness optimization, IEEE/ASME Transactions on Mechatronics 23 (2) (2018) 690–701.

[42] J. Lamaury, M. Gouttefarde, Control of a large redundantly actuated cable-suspended parallel robot, in: Proc. IEEE Int. Conf. Robotics and Automation (ICRA), Karlsruhe, Germany, 2013, pp. 4659–4664.

[43] W. Kraus, V. Schmidt, P. Rajendra, A. Pott, Load identification and compensation for a cable-driven parallel robot, in: Proc. IEEE Int. Conf. Robotics and Automation (ICRA), Karlsruhe, Germany, 2013, pp. 2470–2475.

[44] W. Kraus, V. Schmidt, P. Rajendra, A. Pott, System identification and cable force control for a cable-driven parallel robot with industrial servo drives, in: Proc. IEEE Int. Conf. Robotics and Automation (ICRA), Hong Kong, China, 2014, pp. 5921–5926.

[45] M. Nahon, G. Gilardi, C. Lambert, Dynamics/control of a radio telescope receiver supported by a tethered aerostat, Journal of Guidance, Control, and Dynamics 25 (6) (2002) 1107–1115.

[46] B. Zi, B. Y. Duan, J. Du, H. Bao, Dynamic modeling and active control of a cable-suspended parallel robot, Mechatronics 18 (2008) 1–12.

[47] D. Q. Nguyen, M. Gouttefarde, O. Company, F. Pierrot, On the simplifications of cable model in static analysis of large-dimension cable-driven parallel robots, in: Proc. IEEE/RSJ Int. Conf. Intelligent Robots and Systems (IROS), Tokyo, Japan, 2013, pp. 928–934.

[48] ISO 4308-1:3003(E), Cranes and lifting appliances - selection of wire ropes - part 1: General.

[49] N. Riehl, M. Gouttefarde, C. Baradat, F. Pierrot, On the determination of cable characteristics for large dimension cable-driven parallel mechanisms, in: IEEE Int. Conf. on Robotics and Automation (ICRA), Alaska, USA, 2010, pp. 4709–4714.

[50] J. Du, H. Bao, X. Duan, C. Cui, Jacobian analysis of a long-span cable-driven manipulator and its application to forward solution, Mechanism and machine theory 45 (2010) 1227–1238.

[51] R. J. Caverly, J. R. Forbes, Dynamic modeling and noncollocated control of a flexible planar cable-driven manipulator, IEEE Transactions on Robotics 30 (6) (2014) 1386–1397.

[52] J. Du, S. K. Agrawal, Dynamic modeling of cable-driven parallel manipulators with distributed mass flexible cables, ASME Journal of Vibration and Acoustics 137 (2015) 1–8.

[53] H. Yuan, E. Courteille, M. Gouttefarde, P.-E. Hervé, Vibration analysis of cable-driven parallel robots based on the dynamic stiffness matrix method, Journal of Sound and Vibration 394 (2017) 527–544.

[54] H. Irvine, Cable Structures, MIT Press, Cambridge, 1981.

[55] M. Gouttefarde, J.-F. Collard, N. Riehl, C. Baradat, Simplified static analysis of large-dimension parallel cable-driven robots, in: IEEE International Conference on Robotics and Automation (ICRA), St Paul, Minnesota, 2012, pp. 2299–2305.

[56] T. Dallej, M. Gouttefarde, N. Andreff, R. Dahmouche, P. Martinet, Vision-based modeling and control of large-dimension cable-driven parallel robots, in: IEEE International Conference on Intelligent Robots and Systems (IROS), Vilamoura, Algarve, Portugal, 2012.

[57] A. Fortin-Côté, P. Cardou, A. Campeau-Lecours, Improving cable driven parallel robot accuracy through angular position sensors, in: Proc. IEEE/RSJ Int. Conf. Intelligent Robots and Systems (IROS), Daejeon, Korea, 2016, pp. 4350–4355.

[58] H. Jamshidifar, A. Khajepour, B. Fidan, M. Rushton, Kinematically-constrained redundant cable-driven parallel robots: Modeling, redundancy analysis, and stiffness optimization, IEEE/ASME Transactions on Mechatronics 22 (2) (2017) 921–930.

[59] C. Samson, M. Leborgne, B. Espiau, Robot Control: The Task Function approach, Oxford Engineering Series, 22, Oxford University Press, 1991.

[60] M. Gouttefarde, J.-F. Collard, N. Riehl, C. Baradat, Geometry selection of a redundantly actuated cable-suspended parallel robot, IEEE Transactions on Robotics 31 (2) (2015) 501–510.

[61] C. Gramkow, On averaging rotations, Int. Journal on Computer Vision 42 (1–2) (2001) 7–16.

[62] M. Maher, Means and averaging in the group of rotations, SIAM Journal on matrix analysis and applications 24 (1) (2001) 1–16.

[63] E. Marchand, F. Spindler, F. Chaumette, VISP for visual servoing: a generic software platform with a wide class of robot control skills, IEEE Robotics and Automation Magazine, Special Issue on Software Packages for Vision-Based Control of Motion, P. Oh, D. Burschka (Eds.) 12 (4) (2005) 40–52.

[64] S. Benhimane, E. Malis, Homography-based 2D visual servoing, in: IEEE International Conference on Robotics and Automation (ICRA), Orlando, USA, 2006, pp. 2397–2402.

[65] W. J. Wilson, C. C. Williams Hulls, G. S. Bell, Relative end-effector control using cartesian position-based visual servoing, IEEE Transactions on Robotics and Automation 12 (5) (1996) 684–696.

[66] P. Martinet, N. Daucher, J. Gallice, M. Dhome, Robot control using 3D monocular pose estimation, in: Proceedings of the Workshop on New Trends in Image Based Robot Servoing, IEEE/RSJ International Conference on Intelligent Robots and Systems (IROS), Grenoble, France, 1997, pp. 1–12.

[67] E. Malis, F. Chaumette, S. Boudet, 2 1/2 D visual servoing, IEEE Trans. on Robotics 15 (2) (1999) 238–250.

[68] B. Thuilot, P. Martinet, L. Cordesses, J. Gallice, Position based visual servoing: keeping the object in the field of vision, in: IEEE International Conference on Robotics and Automation (ICRA), Washington, USA, 2002, pp. 1624–1629.

[69] E. Ozgür, N. Andreff, R. Dahmouche, P. Martinet, High speed parallel kinematic manipulator state estimation from legs observation, in: IEEE/RSJ International Conference on Intelligent Robots and Systems (IROS), Tokyo, Japan, 2013, pp. 426–429.

[70] T. Dallej, H. Hadj Abdelkader, N. Andreff, P. Martinet, Kinematic calibration of a gough-stewart platform using and

omnidirectional camera, in: Proceedings of the IEEE International Conference on Intelligent Robots and Systems (IROS), Beijing, China, 2006, pp. 4666–4671.

[71] J.-P. Merlet, Checking the cable configuration of cable-driven parallel robots on a trajectory, in: Proc. IEEE Int. Conf. Robotics and Automation (ICRA), Hong Kong, China, 2014, pp. 1586–1591.

[72] E. Malis, P. Rives, Robustness of image-based visual servoing with with respect to depth distribution errors, in: IEEE International Conference on Robotics and Automation, Vol. 1, Taipei, Taiwan, 2003, pp. 1056–1061.